



Article (refereed) – Published version

Hopkins, Joanne E.; Stephenson, Gordon R.; Green, J. Mattias; Inall, Mark E.. 2014 Storms modify baroclinic energy fluxes in a seasonally stratified shelf sea: inertial-tidal interaction. *Journal of Geophysical Research: Oceans*, 119 (10). 6863-6883. [10.1002/2014JC010011](https://doi.org/10.1002/2014JC010011)

This version available at <http://nora.nerc.ac.uk/506935/>

NERC has developed NORA to enable users to access research outputs wholly or partially funded by NERC. Copyright and other rights for material on this site are retained by the rights owners. Users should read the terms and conditions of use of this material at <http://nora.nerc.ac.uk/policies.html#access>

AGU Publisher statement: An edited version of this paper was published by AGU. Copyright (2014) American Geophysical Union. Further reproduction or electronic distribution is not permitted.

Hopkins, Joanne E.; Stephenson, Gordon R.; Green, J. Mattias; Inall, Mark E.. 2014 Storms modify baroclinic energy fluxes in a seasonally stratified shelf sea: inertial-tidal interaction. *Journal of Geophysical Research: Oceans*, 119 (10). 6863-6883. [10.1002/2014JC010011](https://doi.org/10.1002/2014JC010011)

To view the published open abstract, go to <http://dx.doi.org/10.1002/2014JC010011>

Contact NOC NORA team at
publications@noc.soton.ac.uk



RESEARCH ARTICLE

10.1002/2014JC010011

Storms modify baroclinic energy fluxes in a seasonally stratified shelf sea: Inertial-tidal interaction

Joanne E. Hopkins¹, Gordon R. Stephenson Jr.², J. A. M. Green², Mark E. Inall³, and Matthew R. Palmer¹¹National Oceanography Centre, Liverpool, UK, ²School of Ocean Sciences, Bangor University, Bangor, UK, ³Scottish Association for Marine Science, Oban, UK

Key Points:

- Internal wavefield energy fluxes in a stormy, stratified shelf sea
- Inertial-tidal interaction enhances on-shelf internal wave energy transport
- Two distinct shear and flux regimes: tidal and inertial

Correspondence to:

J. E. Hopkins,
j.hopkins@noc.ac.uk

Citation:

Hopkins, J. E., G. R. Stephenson, J. A. M. Green, M. E. Inall, and M. R. Palmer (2014), Storms modify baroclinic energy fluxes in a seasonally stratified shelf sea: Inertial-tidal interaction, *J. Geophys. Res. Oceans*, 119, 6863–6883, doi:10.1002/2014JC010011.

Received 3 APR 2014

Accepted 9 SEP 2014

Accepted article online 18 SEP 2014

Published online 16 OCT 2014

Abstract Observations made near the Celtic Sea shelf edge are used to investigate the interaction between wind-generated near-inertial oscillations and the semidiurnal internal tide. Linear, baroclinic energy fluxes within the near-inertial (f) and semidiurnal (M_2) wave bands are calculated from measurements of velocity and density structure at two moorings located 40 km from the internal tidal generation zone. Over the 2 week deployment period, the semidiurnal tide drove 28–48 $W m^{-1}$ of energy directly on-shelf. Little spring-neap variability could be detected. Horizontal near-inertial energy fluxes were an order of magnitude weaker, but nonlinear interaction between the vertical shear of inertial oscillations and the vertical velocity associated with the semidiurnal internal tide led to a 25–43% increase in positive on-shelf energy flux. The phase relationship between f and M_2 determines whether this nonlinear interaction enhances or dampens the linear tidal component of the flux, and introduces a 2 day counter-clockwise beating to the energy transport. Two very clear contrasting regimes of (a) tidally and (b) inertially driven shear and energy flux are captured in the observations.

1. Introduction

The oceans' rich internal wavefield is an essential link in the energy cascade from large to small-scale motions and is a major source of energy available for vertical mixing. In the oceans' interior, dissipation of low-mode internal wave energy provides deep mixing that is crucial in maintaining the Meridional Ocean Circulation (see, e.g., the reviews by Garrett [2003] and Wunsch and Ferrari [2004]). Elsewhere, in shallow shelf seas, vertical mixing across the seasonal thermocline maintains elevated summer time production [Sharples *et al.*, 2007; Pingree and Mardell, 1981], helping continental shelves to provide 15–30% of total oceanic primary production [Wollast, 1998; Muller-Karger *et al.*, 2005], despite only accounting for $\approx 5\%$ of the global ocean area. Temperate shelf seas are therefore a significant CO_2 sink [Thomas *et al.*, 2004; Borges *et al.*, 2005], and a critical link in the ocean-earth-atmosphere system.

Freely propagating internal gravity waves, supported by density gradients within the ocean interior, occupy a frequency range bounded below by the local inertial frequency ($f = 2\Omega \sin(\phi) = \frac{1}{15.9}$ cycles h^{-1} at a latitude $\phi = 48.7^\circ N$), and at the higher end by the local buoyancy frequency, N . The two most energetic parts of the global internal wave spectrum are near-inertial waves with frequencies $\omega \approx f$ and the lunar semidiurnal frequency, M_2 . Using measurements made in the field, this paper describes (1) interactions between near-inertial waves and the semidiurnal internal tide and (2) the resulting energy fluxes in the wave band bounded by these frequencies in the Celtic Sea, a seasonally stratified section of the Northwest European Shelf (Figure 1).

The flux of internal wave energy past a given location provides an upper bound on the amount of energy available for dissipation and subsequent turbulent mixing across the shelf. Model parameterizations of the rate of dissipation, many based on energy transfer from large to small scales through wave-wave interactions and the evolving vertical shear structure, are not yet fully capable of reproducing the magnitude and episodic nature of turbulent events within the seasonal pycnocline [MacKinnon and Gregg, 2003a; Gregg, 1989; Polzin *et al.*, 1995]. A focus here on the existence, impact, and physical mechanism behind tidal-inertial wave coupling in the context of energy fluxes is therefore highly relevant to ongoing developments of these parameterizations.

This is an open access article under the terms of the Creative Commons Attribution License, which permits use, distribution and reproduction in any medium, provided the original work is properly cited.

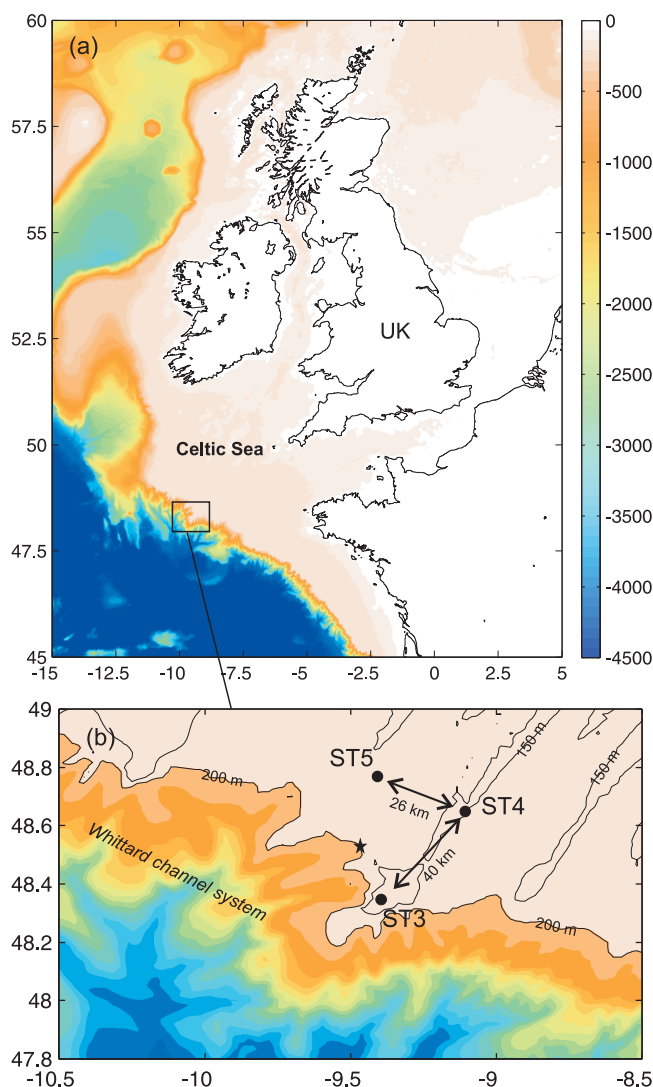


Figure 1. (a) Bathymetry (m) of the Northwest European Shelf. (b) Location of moorings ST3, ST4, and ST5. The 200 m (shelf edge) and 150 m depth contours are marked. The black star marks the location of flux estimates made by Green et al. [2008] referred to in the discussion.

Semidiurnal internal waves are primarily generated by tidal flow over steep topography and remove energy from the barotropic tide [Munk and Wunsch, 1998; Egbert and Ray, 2001]. Some of the largest internal tides are formed mid-ocean over the Hawaiian and Macquarie Ridges [Carter et al., 2008; Lee et al., 2006] and across the Luzon Strait [Lien et al., 2005; Ramp et al., 2010], but continental slopes such as the Australian Northwest shelf [Holloway, 2001], the New Jersey shelf [Shroyer et al., 2010], the Malin shelf [Rippeth and Inall, 2002], the Monterey Bay area [Kang and Fringer, 2012], and the shelf edge of Northeast New Zealand [Sharples et al., 2001] also act as internal tide generators. In his 1982 work, Baines classified the Northwest European shelf, alongside the East and South China Seas, the Guiana Basin region, the Australian Northwest shelf, and the Gulf of Maine-Grand Banks region, as one of the most globally significant hot spots for tidal energy conversion and flux [Baines, 1982], a statement still valid today. Recently, the highest amplitude internal solitary wave (105 m) ever observed in the Celtic Sea has been reported and successfully modeled [Vlasenko et al., 2014]. The linear internal tide generated here has been observed to propagate coherently up to 170 km onto the shelf [Inall et al., 2011]. However, the shoreward energy decay scale is estimated to be 42 km, implying that little of the energy generated directly

at the shelf break is available for inner shelf mixing and subsequent maintenance of the subsurface chlorophyll maximum [e.g., Sharples et al., 2007].

Inertial oscillations and near-inertial waves are predominately generated by wind events. The response of the surface ocean to wind energy input at a broad band of frequencies is initially at $\omega = f$. This energy is subsequently spread over a narrow frequency band surrounding f , typically $\approx 0.1f$ wide, by mesoscale ocean processes [see van Haren, 2004, and references therein]. In the open ocean, convergences and divergences of inertial surface motion can force near-inertial disturbances downward into the interior [Alford, 2003; Alford et al., 2012], providing a deep ocean energy flux comparable to that of the internal tide [Alford, 2003]. In the coastal ocean, changes in sea surface elevation at the coast drive inertial oscillations beneath the thermocline that are 180° out of phase with the those at the surface [Rippeth et al., 2002]. This phase shift gives rise to a maximum in inertial shear across the thermocline and short-lived shear spikes that provide a mid-shelf source of energy for mixing and may increase the daily nitrate flux into the subsurface chlorophyll maximum by a factor of 17 [Rippeth et al., 2009; Williams et al., 2013]. In tideless environments, such as the Baltic Sea, near-inertial motions drive enhanced dissipation rates that are the major source of mixing in deep water [van der Lee and Umlauf, 2011; Holtermann and Umlauf, 2012]. Where stratification intersects

Table 1. Mooring Locations, Depths, and Instrumentation Setup

	ST4	ST5
Position	48° 38.908' N, 09° 06.363' W	48° 46.138' N, 09° 24.378' W
Mean depth (m)	156	169
Deployment	16–28 Jun 2012 (11.9 days)	13–29 Jun 2012 (15.7 days)
ADCP	150 kHz Flowquest 2 m bins, 1 min ensembles 60 pings per ensemble	150 kHz RDI 2.5 m bins, 2 min ensembles 30 pings per ensemble
T chain	1 min sampling SBE37 microcats with CTD at 8, 30, 40, 50, 135, 155 m 22 Star-Oddi mini-temperature loggers between 11 and 119 m, spaced by 2–10 m (pycnocline-bottom)	1 min sampling SBE microcats with CTD at 14, 38, 48, 58, 156 and 169m 19 Star-Oddi mini-temperature loggers between 16 and 140 m, spaced by 2–20 m (pycnocline-bottom)

topography, the upwelling and downwelling associated with oscillatory inertial flow gives rise to the generation of near-inertial internal waves at frequencies slightly above the inertial period [Tintore *et al.*, 1995; Davies and Xing, 2003]. These superinertial waves are then able to freely propagate horizontally and transport energy. The contribution that near-inertial waves and oscillations make to baroclinic energy fluxes in shelf seas however has received little attention.

Near-inertial and semidiurnal tidal currents do not operate in isolation. In fact, the Earth's rotation features in Laplace's tidal equations, so the barotropic tide propagates as an inertia-gravity wave. There is already evidence to suggest that near-inertial oscillations can regulate and modify the internal wavefield, both through linear and nonlinear interaction. For example, Shroyer *et al.* [2011] hypothesize that the amplitude of nonlinear internal waves (NLIW) may be impacted by the linear phasing in and out of near-inertial and semidiurnal motions, and the associated near-inertial shear constructively and destructively modulating the nonlinearity of wave evolution. Peaks at the $M_2 + f$ frequency, the sum frequency of inertial and semidiurnal motions, in both open ocean [Mihaly *et al.*, 1998] and shallow sea environments [van Haren *et al.*, 1999] provide further evidence of internal tide and wind-induced energy coupling. More generally, nonlinear wave-wave interactions [Muller *et al.*, 1986] mean that energy can be cascaded to higher frequencies and ultimately irreversible mixing [Garrett, 2001].

The overarching aim of this paper is to investigate whether wind energy input into the surface of the ocean is able to enhance the on-shelf fluxes of linear baroclinic internal tidal energy generated at the shelf edge in a seasonally stratified shelf sea. We use our observations to quantify independent energy fluxes within the semidiurnal and near-inertial wave bands, and subsequently fluxes resulting from interactions between oscillations at these two frequencies. Our findings of increased horizontal transport of energy through the system during periods of strong inertial oscillations, and resolution of the spatial and temporal distribution of this extra energy is explained by nonlinear coupling between vertical inertial shear and semidiurnal vertical velocities.

2. Data Collection and Processing

Data used here were collected in the Celtic Sea, the widest section of the Northwest European Shelf (Figure 1a), as part of the UK FASTNET project (Fluxes Across Sloping Topography of the North East Atlantic). Typical water depths range between 100 and 150 m and drop rapidly beyond the 200 m shelf edge contour to over 2000 m. The 500 km stretch of steep shelf edge is incised with over 30 deep and narrow canyons [Zaragosi *et al.*, 2006], which generate a highly complex three-dimensional baroclinic internal wavefield [Vlasenko *et al.*, 2014].

Our study site was located within the eastern branch of the Whittard channel system (Figure 1b). Two moorings were deployed 26 km apart and 40 km on-shelf from the 200 m shelf edge contour for 11.9 and 15.7 days in June 2012. These moorings were well away from the internal tide generation zone, a problem which has caused bias in previous descriptions of the internal wavefield in the area [e.g., Green *et al.*, 2008]. Both moorings, ST4 and ST5, consisted of full water column temperature chains and bottom mounted 150 kHz ADCPs recording full water column currents. A minimum of 2.5 m vertical bins and 2 min current ensembles, together with 1 min sampling from the temperature loggers (spaced 2 m apart across the pycnocline

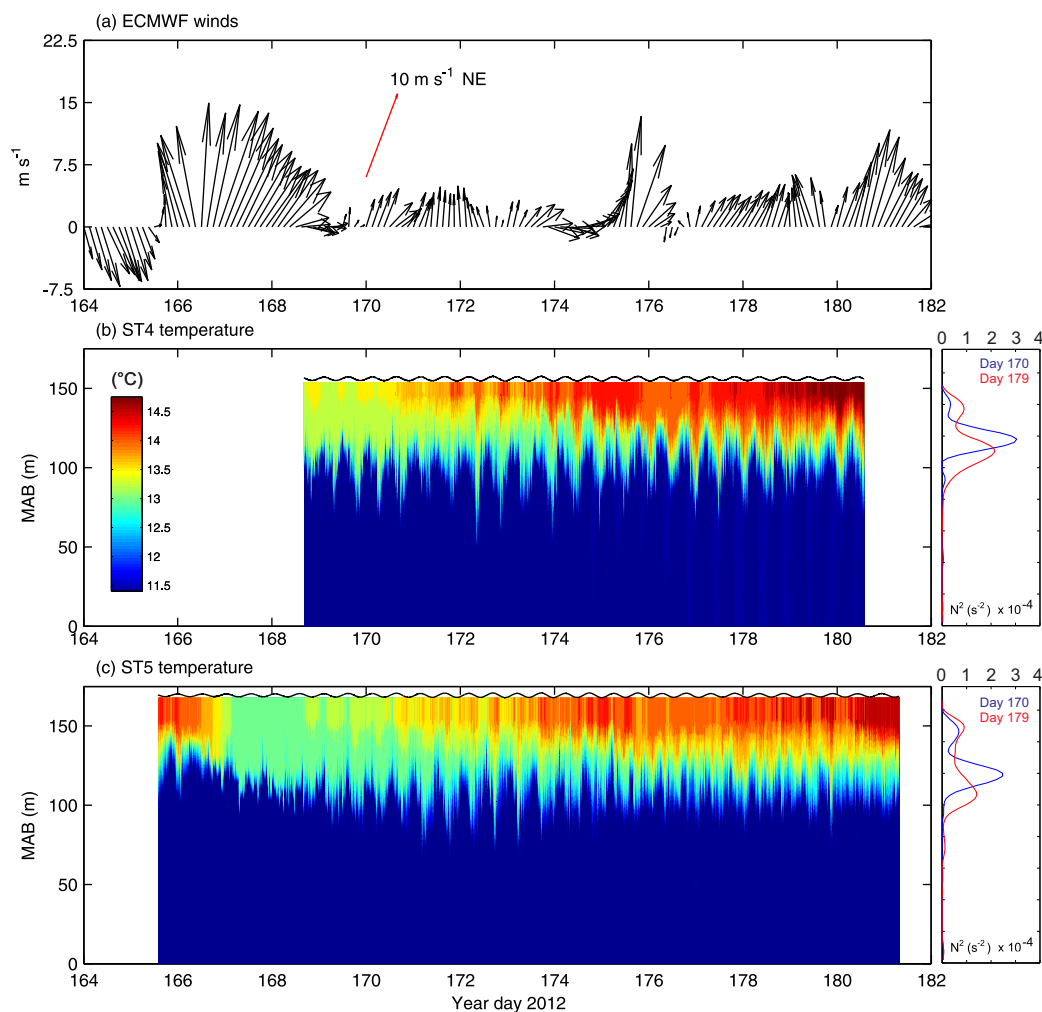


Figure 2. (a) Wind speed and direction from ECMWF ERA-Interim. (b and c) Temperature at ST4 and ST5 ($^{\circ}\text{C}$). Plots to the right show the buoyancy frequency (N^2) on days 170 (blue) and 179 (red). Note that vertical heave of isopycnals caused by the passage of internal waves accounts for differences in the depth of maximum N^2 between the two profiles.

and 5–20 m apart in the surface and bottom layers), allows us to resolve the entire frequency range for internal waves, from the inertial to the buoyancy frequency. Table 1 provides full details of mooring instrumentation and setup at ST4 and ST5. A third mooring, ST3, consisting only of a bottom mounted 150 kHz ADCP provided full water column currents nearer the shelf edge (Figure 1b). Our date convention is such that yearday 1.5 is noon on the 1 January 2012.

All temperature loggers were cross calibrated before and after deployment to correct for any drifts and offsets. Additionally, all the Star-Oddi mini-temperature loggers were calibrated against the ship's CTD (a Seabird *9plus*). Velocity measurements in bins in which less than 100% of pings were recorded as good were rejected and filled using a vertical linear interpolation. A third-order low-pass Butterworth filter with a cutoff frequency of $\frac{1}{0.05}$ cycles m^{-1} was applied to each velocity profile to reduce noise, and current direction at each mooring was corrected for magnetic variation (-4.3° and -4.4° at ST4 and ST5, respectively). Temperature and current measurements were linearly interpolated onto coincident $1 \text{ min} \times 2 \text{ m}$ resolution grids. The top 12 and 21 m of current measurements were rejected at ST4 and ST5, respectively, owing to contamination by strong sea surface echos. Given the predominately mode-1 current structure and a mid-pycnocline depth ($\sigma = 1027 \text{ kg m}^{-3}$) that varied between 40 and 80 m (see section 3), it was appropriate to perform a nearest neighbor interpolation using the last good ADCP bin to complete the velocity profiles. The bottom 7 m was similarly estimated using the first good ADCP bin above the seabed. At each mooring, conductivity, temperature, and pressure were measured at six depths throughout the water column (see Table 1). Full water column profiles of salinity were therefore constructed using a linear three-dimensional

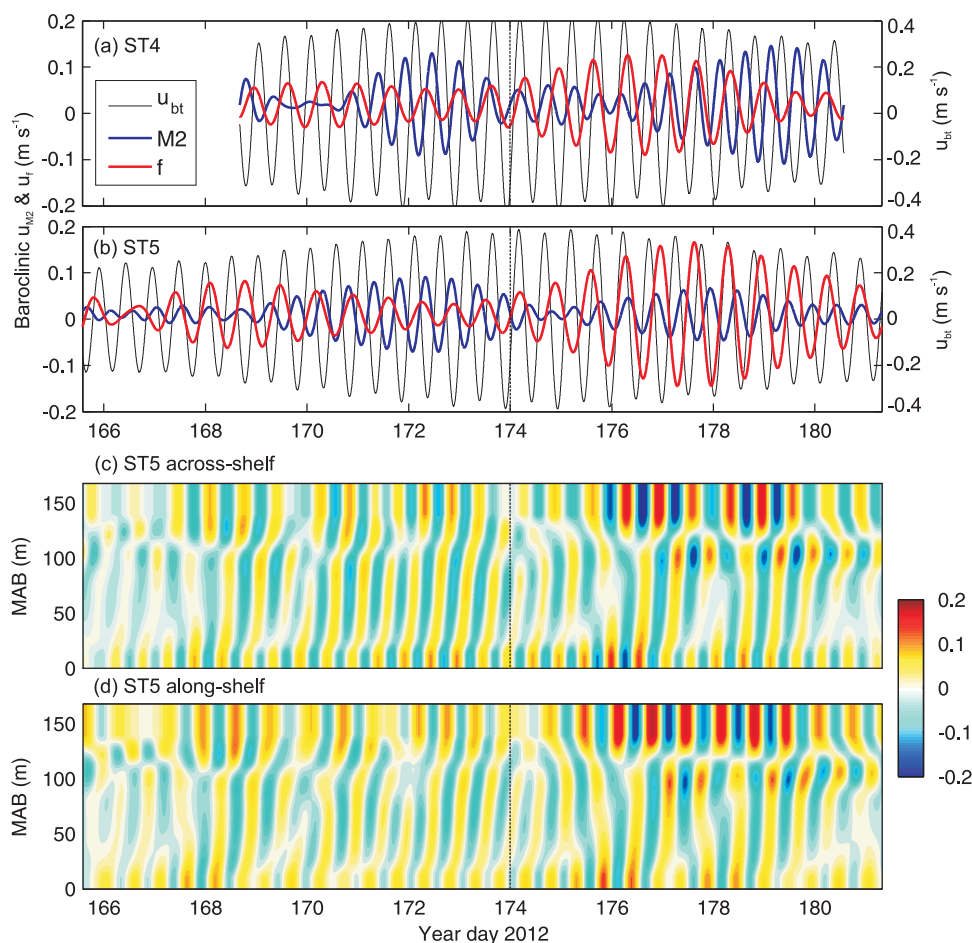


Figure 3. (a) Across-shelf baroclinic currents from ST4 at 15 m depth band passed about the M_2 ($\frac{1}{11.2} - \frac{1}{14.3}$ cycles h^{-1}) (blue) and inertial ($\frac{1}{14.3} - \frac{1}{18.3}$ cycles h^{-1}) (red) frequencies. Across-shelf barotropic tidal currents in black. (b) As above for ST5. (c) Across and (d) along-shelf baroclinic currents ($m s^{-1}$) at ST5 band passed between $1/11.2$ and $1/18.3$ cycles h^{-1} . Vertical dashed lines indicate spring tides.

interpolation function. First, using simultaneous recordings of temperature and salinity, a surface of the form $salinity = F(temperature, time)$ was fitted. Delaunay triangulation was then used to evaluate the salinity at instances where only temperature (and of course time) was measured. Although temperature is the leading order control on density during the summer in the Celtic Sea, a reliance on the accuracy of density perturbations in calculations of energy flux, coupled with some appreciable variability in salinity throughout the deployment, favored calculation of density using this salinity “reconstruction.”

3. Winds, Stratification, and Currents

3.1. Meteorological Conditions

Throughout the deployment, a number of strong wind events, associated with the passage of low-pressure systems, provided a range of wind stress conditions (Figure 2a). The first storm, starting on day 166, lasted 2.5 days and at its peak drove wind speeds in excess of $20 m s^{-1}$ (recorded by the ships anemometer). A second, more impulsive, wind event on day 175 peaked at $15 m s^{-1}$ and developed just as rapidly, but died away in less than a day. The wind direction was predominately northeast and outside of storms averaged $5 m s^{-1}$.

3.2. Water Column Structure

Coincident with the peak of the first storm on day 167, the thermocline deepens from 40 to 60 m, and surface waters cool by $1.1^\circ C$ (Figures 2b and 2c). During the following days, there is a sharp thermocline with squared buoyancy frequency $N^2 = -\frac{g}{\rho_0} \frac{d\rho}{dz} = 2.5-3 \times 10^{-4} s^{-2}$ (blue profiles in Figures 2b and 2c insets), where

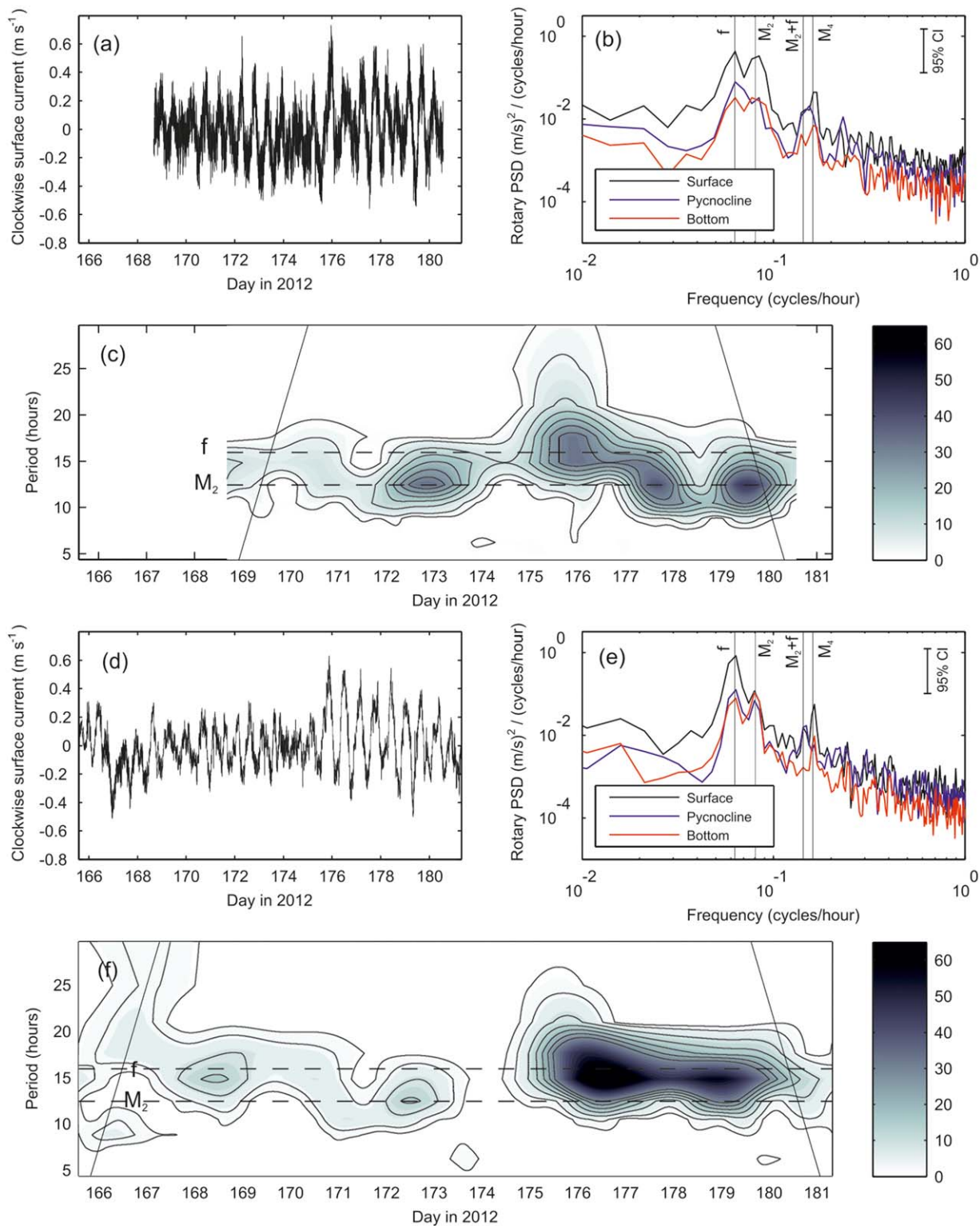


Figure 4. Clockwise baroclinic currents at 15 m depth at (a) ST4 and (d) ST5. Power spectra of baroclinic currents at the surface (15 m depth), pycnocline (defined as the mean depth of the 1027 kg m⁻³ isopycnal), and near bed (40 m above the bottom) at (b) ST4 and (e) ST5. Only the dominant clockwise components are shown. Rotary spectra were calculated using a Welch's periodogram with a 7.9 h hanning window and 50% overlap. Spectral resolution of 0.0053 cycles h⁻¹. Note that the time series are different lengths. Wavelet power spectra of the clockwise surface baroclinic currents at (c) ST4 and (f) ST5. Power units are (m s⁻¹)². The Cone of Influence, outside of which calculation of the power becomes uncertain, is marked by the thin lines.

Table 2. Summary of the Main Wave and Interaction Frequencies Discussed Here and the Corresponding Notations Used

Frequency		Period (h)	Energy Source
M_2	Semidiurnal IT	12.42	Barotropic tide
$M_4 (= M_2 + M_2)$	Shallow water quarter-diurnal Over tide	6.22	Nonlinear M_2 Self interaction
f	Inertial	15.93	Wind
$M_2 + f$	Tidal-inertial interaction frequency	6.98	Nonlinear interaction
$M_2 - f$	Tidal-inertial interaction frequency	56.37	Isopycnal heave (linear interaction)

g is acceleration due to gravity, ρ the potential density, and ρ_0 the mean potential density between two layers. Surface temperatures are reestablished by day 176 ($> 14^\circ\text{C}$) and a broader, more diffuse thermocline is present with a lower N^2 of $1.5\text{--}2.25 \times 10^{-4} \text{ s}^{-2}$. Semidiurnal thermocline displacements of up to 55 m (peak-to-trough) at ST4 dominate the time series, visually demonstrating the importance of the M_2 internal

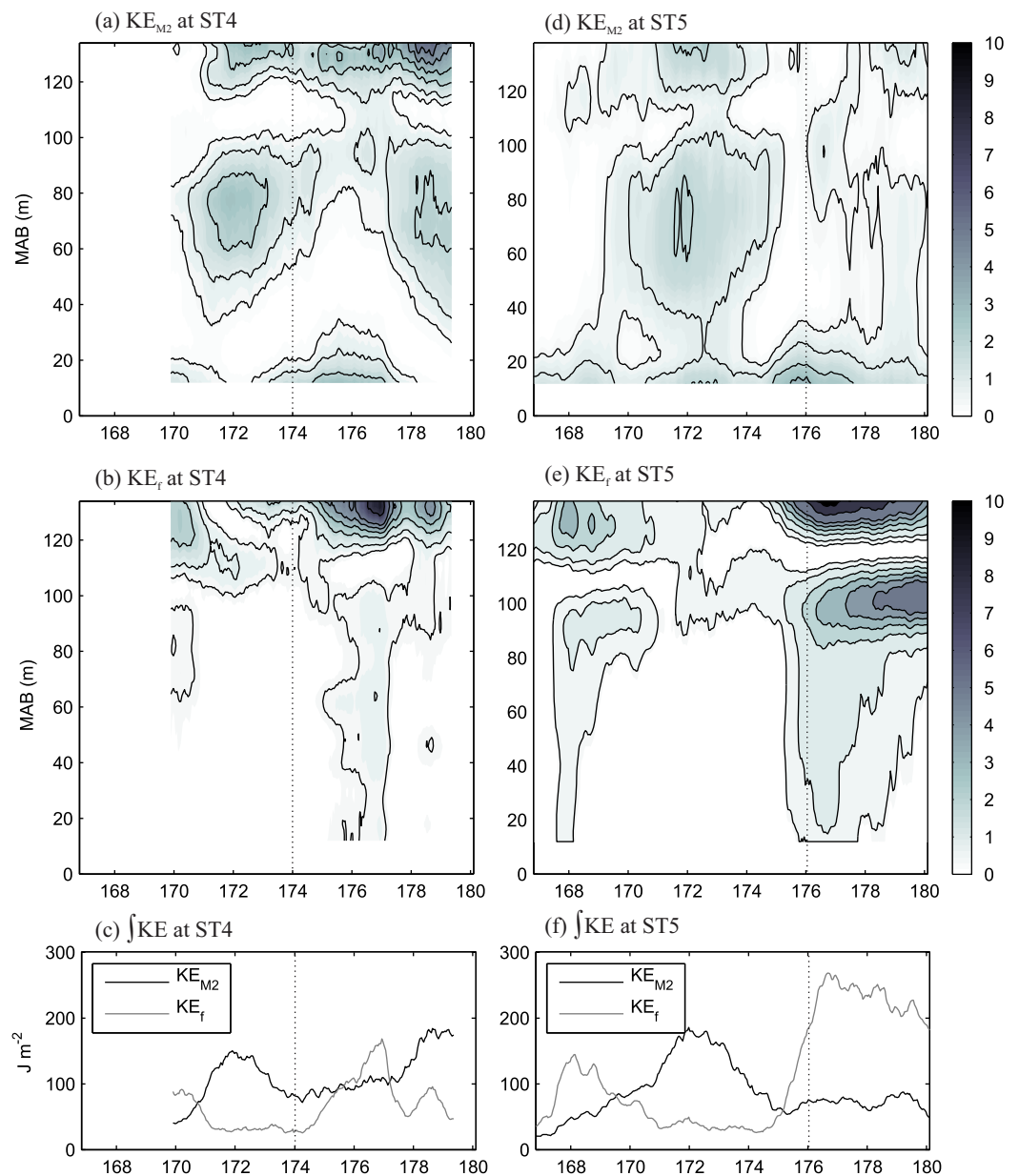


Figure 5. Semidiurnal and inertial kinetic energy at (a and b) ST4 and (d and e) ST5 in J m^{-3} . (c and f) Depth-integrated kinetic energy (J m^{-2}). Vertical dashed lines indicate spring tides.

tide. High-amplitude (up to 40–50 m), high-frequency wave packets are also clearly visible within the troughs of the M_2 waves. Spectral analysis of the temperature within the surface layer, thermocline, and near the bed at both sites (not shown) reveals pronounced energy peaks at M_2 and at the shallow water over tides M_4 and M_6 . Using the buoyancy profiles (N^2) in Figure 2, and solving the wave equation $\frac{\partial^2 w}{\partial z^2} + \left(\frac{N^2 - \sigma^2}{\sigma^2 - f^2}\right) k^2 w = 0$, where f is the inertial frequency, k the horizontal wave number, w the vertical perturbation at depth z , and σ the wave frequency, dynamical mode estimates of the mode-1 phase speed (c) and wavelength (λ) of the semidiurnal internal tide are $c = 0.5\text{--}0.6 \text{ m s}^{-1}$ and $\lambda = 25\text{--}27 \text{ km}$, respectively.

3.3. Currents

Tidal analysis using six constituents (M_2 , S_2 , N_2 , O_1 , K_1 , M_4) shows barotropic tidal currents to be dominated by a clockwise semidiurnal tide with M_2 semimajor axis amplitudes of 0.37 and 0.33 m s^{-1} at ST4 and ST5, respectively. The major axes are oriented at 16° and 41° , respectively (clockwise from north), which is approximately across shelf. Baroclinic currents are calculated by subtraction of the depth mean which is taken as the barotropic tide. Maximum spring tidal currents of 0.4 m s^{-1} occurred on day 174, half way through our deployment (Figure 3). Here we rotate our coordinate system 58° counter clockwise, aligning the x axis (u -velocity component) across shelf (positive NNE), and the y axis (v -velocity component), along shelf (positive WNW).

Baroclinic currents within the near-inertial to semidiurnal band have a predominately mode-1 vertical structure (Figures 3c and 3d), with surface and subpycnocline currents for the most part 180° of out phase. This is confirmed by EOF analysis of the unfiltered time series where the first EOF mode, with one zero crossing at 48–58 m depth explains 65% and 75% of the variance in across and along-shelf baroclinic currents at ST5 (45% and 47% at ST4, respectively). Additionally, a well-defined second EOF mode, with two zero crossing points at depths of 20–35 and 104–119 m in the across, and along-shelf directions at both sites, accounting for between 11% and 16% of the variance, may be interpreted as the existence of a mode-2 baroclinic wave.

Although a short record, modulation in the intensity of semidiurnal baroclinic currents is not well correlated to the strength of the barotropic tide at either site. Approaching spring tides, above the pycnocline internal tidal currents increase steadily between days 170 and 173 (up to 0.1 m s^{-1} in an across-shelf direction) and are stronger than inertial currents (Figures 3a and 3b). Post day 173, however, there is a sudden and somewhat unexpected drop in M_2 amplitudes. Coincidentally, the strength of near-inertial oscillations increases (up to 0.15 m s^{-1}) and for a short while (about 1 day at each site), almost entirely dominate the record. Despite this sudden generation of inertial motion in response to the wind event on day 174, one might expect a clearer spring-neap M_2 internal tidal current envelope to exist. The sharp transition from M_2 to f dominance is punctuated by a drop in energy within both of these wave bands on day 174 (Figures 4c and 4f).

There are peaks in baroclinic energy near the inertial-tidal interaction frequency $M_2 + f$ ($=6.98 \text{ h}$) within the pycnocline and surface waters at both sites (Figures 4b and 4e). Alford [2001] shows that spectral peaks at interaction frequencies can arise from near-inertial motions being heaved up and down by tidal displacement. The pycnocline spectra, recalculated by taking currents along the 1027 kg m^{-3} isopycnal (i.e., within a semi-Lagrangian frame), maintains a distinct clockwise peak at $M_2 + f$, providing evidence that this energy peak has arisen through nonlinear interaction, where energy is transferred from the near-inertial and tidal peaks to different frequencies, and is not therefore an artifact of pycnocline heaving. A counter-clockwise peak within the pycnocline currents near $M_2 - f$ does not persist in the semi-Lagrangian frame (not shown), suggesting that it results from a linear process. To provide clarity throughout our discussions, Table 2 summarizes the main wave and interaction frequencies and the notations that we adopt when referring to them.

4. Baroclinic Kinetic Energy

As a means of further assessing and comparing energy within the dominant M_2 and inertial bands, we calculate the baroclinic kinetic energy (KE). After subsampling the velocity record by forming 10 min averages of the baroclinic currents every hour, harmonic analysis was carried out at each depth for periods of 12.42 (M_2) and 15.93 (inertial) h. Since the beat frequency between M_2 and f is 56.4 h, these fits were performed

within 58 h windows. For each window, the time-averaged vertical profile of KE was calculated for the two frequencies using:

$$KE(z) = \frac{1}{2} \rho [\overline{u(z)^2} + \overline{v(z)^2}], \quad (1)$$

where $KE(z)$ is the profile of either the M_2 or inertial kinetic energy and $\overline{u(z)^2}$ and $\overline{v(z)^2}$ the time-averaged square cross and along-shelf velocity components calculated from the harmonic analysis. For the internal tide kinetic energy, the time average was performed over one tidal cycle, while for the inertial kinetic energy, the average was over one inertial period.

At ST5, inertial kinetic energy peaks on day 168, 2 days after the beginning of the first storm, and has been dissipated by day 170 (Figure 5e), consistent with a decay scale of 2–3 inertial periods. The maximum depth-integrated KE_f resulting from this wind event was 140 J m^{-2} (Figure 5f). Higher-amplitude inertial oscillations following the storm on day 174 (Figures 4a and 4d) lead to a greater and more prolonged increase in KE_f , concentrated within the surface 15–20 m (Figures 5b and 5e). At ST5, the near surface increase is accompanied by a second slightly deeper maximum across the thermocline at 100 mab (meters above bottom). This results in a larger depth-integrated peak in KE_f on day 177 at ST5 (270 J m^{-2}) compared to at ST4 (170 J m^{-2}).

The evolution of semidiurnal kinetic energy at ST4 and ST5 is comparable before day 174. There are surface, mid-water column (between 40 and 100 mab), and near-bed maxima of comparable magnitudes centered on day 172. The depth-integrated KE_{M_2} is 145 and 180 J m^{-2} , respectively (Figures 5a, 5c, 5d, and 5f). On day 174, at maximum spring tides, there is a decrease in KE_{M_2} at both sites. Whereas at ST5, the depth-integrated internal tidal energy stays at $60\text{--}80 \text{ J m}^{-2}$ for the remainder of the deployment, KE_{M_2} at ST4 rises again, peaking on day 179 at 180 J m^{-2} , driven by further pulses in surface and mid-water column energy.

5. Baroclinic Energy Fluxes

The total instantaneous baroclinic linear across-shelf energy flux resulting from the internal wavefield, $F_u = u'p'$, is calculated based on the correlation between velocity and pressure perturbations (u' and p'), following Nash *et al.* [2005]. Assuming that the internal tide is hydrostatic, as the average buoyancy frequency during the deployments, $4 \times 10^{-3} \text{ s}^{-1}$ (≈ 4 min period), was 2 orders of magnitude higher than the dominant M_2 frequency, pressure perturbations are calculated from the hydrostatic equation:

$$p'(z, t) = p_0(t) + g \int_z^0 \rho'(\hat{z}, t) d\hat{z}, \quad (2)$$

where g is the gravitational acceleration constant and p_0 is the surface pressure calculated by requiring that the depth-averaged pressure perturbation be zero, $\frac{1}{H} \int_{-H}^0 p'(z, t) dz = 0$. Density perturbations, ρ' , are calculated by separating the instantaneous density, ρ , into its mean and fluctuating components:

$$\rho'(z, t) = \rho(z, t) - \bar{\rho}(z, t). \quad (3)$$

The mean vertical profile, $\bar{\rho}$, represents the water column in the absence of internal waves. During the deployment, the water column structure varied owing to the passage of a strong wind event. To account for this and help minimize the contribution of low-frequency, mesoscale variability to the perturbations, the overbar quantity was calculated as a running mean over six internal tidal periods. In practice, however, varying this averaging interval between 2 and 8 tidal periods had a minimal impact on the results.

Across-shelf velocity perturbations, u' , were calculated from:

$$u'(z, t) = u(z, t) - \bar{u}(z) - u_0(t), \quad (4)$$

where $\bar{u}(z)$ is the time mean vertical profile, calculated as a running mean over six internal tidal periods, and $u_0(t)$ is an unknown depth average velocity calculated by requiring that the depth-average velocity perturbation be zero, $\frac{1}{H} \int_{-H}^0 u'(z, t) dz = 0$. Along-shelf fluxes, $F_v = v'p'$, are calculated following the same procedure. To ease notation, the subscripts u and v are henceforth dropped and where necessary the distinction between across and along-shelf fluxes is made more descriptively. Flux vectors are denoted by Φ ($= F_u + iF_v$).

Table 3. Deployment Mean Depth-Integrated Fluxes Calculated Over 22 Complete Coincident M₂ Periods (day 168.68–180.06)^a

	ST4	ST5
<i>Vector Fluxes</i> ($\Phi = F_u + iF_v$) ($W m^{-1} \text{ } ^\circ$)		
Φ	65 (275)	37 (357)
Φ_{M_2}	52 (283)	30 (14)
Φ_T	49 (283)	25 (6)
Φ_f	2 (72)	6 (230)
<i>Across-Shelf Flux</i> (F_u) ($W m^{-1}$)		
F	-29	31
F_{M_2}	-17	28
F_T	-16	23
F_f	1	-6
<i>Positive Across-Shelf Flux</i> ($F_u > 0$) ($W m^{-1}$)		
Mean (max)		
F	93 (1275)	118 (1403)
F_{M_2}	28 (100)	48 (193)
F_T	40 (166)	60 (183)
F_f	4 (11)	9 (31)
<i>Along-Shelf Flux</i> (F_v) ($W m^{-1}$)		
F	58	22
F_{M_2}	49	9
F_T	47	11
F_f	-1	2

^aValues in brackets for the vector fluxes represent direction in degrees clockwise from north. Values in brackets for the positive across-shelf fluxes represent the maximum observed.

a 130 m depth range) is 1.098×10^{-4} cycles s^{-1} , which is slightly superinertial. Maximum and minimum values of f_{eff} are $1.03f$ and $0.97f$, respectively.

We also calculate perturbations and flux across a frequency range encompassing both the semidiurnal and near-inertial bands, $1/11.2$ – $1/18.3$ cycles h^{-1} (u'_T and p'_T), allowing any near-inertial-tidal interaction to be assessed. Note that Φ_T is not a summation of the independent linear near-inertial and M₂ fluxes, $\Phi_T \neq \Phi_{M_2} + \Phi_f$, but a quadratic quantity containing cross terms. For the across-shelf component, F_T , may be calculated from:

$$F_T = (u'_{M_2} + u'_f)(p'_{M_2} + p'_f) = u'_{M_2}p'_{M_2} + u'_f p'_f + u'_{M_2}p'_f + u'_f p'_{M_2}. \quad (5)$$

We will return to this later in the discussion. The instantaneous energy fluxes within each band are $F_{M_2} = u'_{M_2}p'_{M_2}$, $F_f = u'_f p'_f$, and $F_T = u'_T p'_T$. Bracket averaging, $\langle F_\omega \rangle_\omega$, is then carried out over integer wave periods, ω , where $\omega = M_2$ or f . Depth integrals, $\int_{-H}^0 \langle F_\omega \rangle_\omega dz$, are also presented. Where deployment mean figures are reported, the same coincident time period for both moorings is used. In all cases, positive across and along-shelf fluxes are NNE (on-shelf) and WNW, respectively.

5.1. Internal Tide Energy Fluxes

At ST4, the internal tide drove a net flux of $52 W m^{-1}$ WNW (283°) along the shelf (Table 3). Just 26 km (one IT wavelength) away at ST5, $30 W m^{-1}$ of energy propagated northward onto the shelf (14°) throughout the deployment. These flux magnitudes represent 80% of the net flux driven by the full baroclinic internal wavefield. At both sites, the majority of flux vectors averaged over integer M₂ periods are oriented within 90° of each other, demonstrating that although different between sites, there is reasonable consistency and stability in the direction of internal tidal fluxes at each location (Figure 6c). The magnitudes of maximum fluxes over a single M₂ period recorded at ST4 and ST5 were 101 and $93 W m^{-1}$, respectively. Considering only the net across-shelf component, $17 W m^{-1}$ is directed off-shelf at ST4, whereas $28 W m^{-1}$ propagates on-shelf at ST5, equating to 59% and 90% of across-shelf energy flux. If only positive across-shelf fluxes are considered, then 28 and $48 W m^{-1}$ are directed on-shelf at ST4 and ST5 over the deployment.

The full temporal and vertical variability is shown in Figures 6a–6c, 7a–7c, and 8a–8c. At both sites, the net flux is off-shelf near the bottom (0.25 – $0.5 W m^{-2}$). At ST4, this is normal to the surface flux, but at ST5 opposite to the northward surface and mid-water column energy transport. The largest fluxes are sustained above the pycnocline and increase toward the surface. There is evidence at both locations of a weaker sub-pycnocline maxima, between 20 and 100 m above the bottom. This mid-water column feature is most

In addition to the total flux, F , estimates for specific frequency bands are made by band pass filtering the relevant perturbation quantities and are calculated here for the near-inertial and semidiurnal bands. Semidiurnal perturbations (u'_{M_2} and p'_{M_2}) were extracted using a band pass between frequencies of $1/11.2$ – $1/14.3$ cycles h^{-1} . A frequency range of $1/14.3$ – $1/18.3$ cycles h^{-1} was used for the near inertial (u'_f and p'_f). These upper and lower limits, $\{0.9, 1.15\}f$, are the same as those used by Alford et al. [2012] to isolate near-inertial velocities. The band extends above and below f to allow for the potential raising and lowering of the “effective” inertial frequency by mesoscale motions. The “effective” inertial frequency, $f_{eff} = f + 0.5\zeta$, where $\zeta = (\frac{\partial v}{\partial x}) - (\frac{\partial u}{\partial y})$ is the low-frequency (<0.75 cycles d^{-1}) potential vorticity, and $\frac{\partial v}{\partial x}$ ($\frac{\partial u}{\partial y}$) the cross- (along) slope gradient of the along- (across) slope low-pass filtered velocity is calculated here using the additional ADCP mooring nearer the shelf edge (ST3 in Figure 1b). The depth and time mean f_{eff} (over

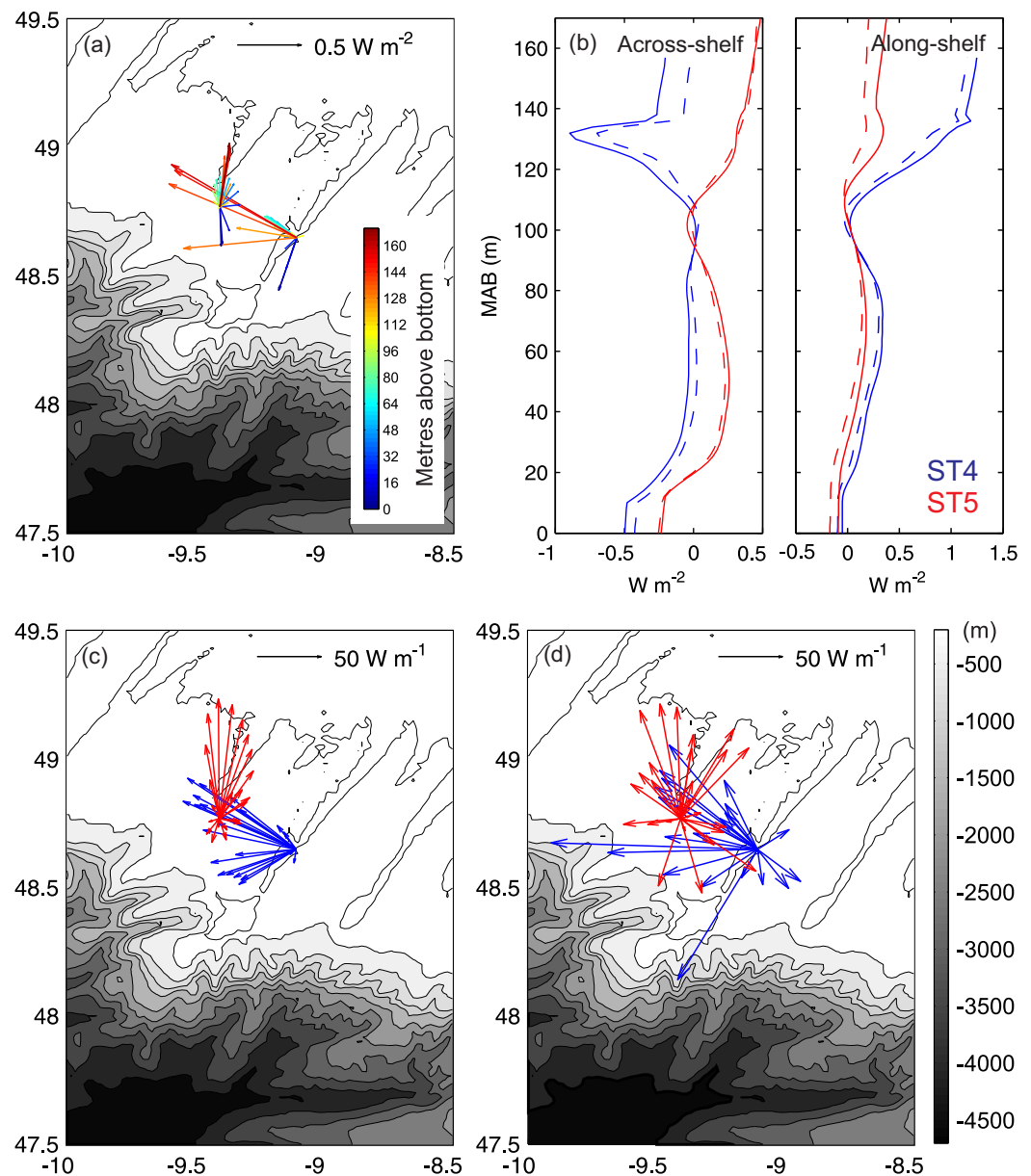


Figure 6. (a) Deployment mean M_2 internal tide energy fluxes at each depth in $W m^{-2}$. (b) Vertical profiles of time mean across and along-shelf fluxes at ST4 (blue) and ST5 (red) for F (solid) and F_{M2} (dashed). Means calculated over 22 coincident M_2 tidal periods. Vectors of depth-integrated energy fluxes (c) $\int_{-H}^0 \langle \Phi_{M2} \rangle_{M2} dz$ and (d) $\int_{-H}^0 \langle \Phi_T \rangle_{M2} dz$ at ST4 (blue) and ST5 (red) in $W m^{-1}$.

prominent between days 170 and 174 at both sites. A second pulse is observed at ST4 on day 178, but is not so evident at ST5. This three-layer structure most likely results from the baroclinic mode-2 internal tide. On day 172, for example, there are two zero crossing points in the across and along-shelf flux at ST5 (Figures 8a and 8b), the first around 110 mab and the second near 25 mab. Aside from an increase in off-shelf energy near the bottom that peaks between days 174 and 176, there is little further evidence of spring-neap variability in the time series, although the record is short.

5.2. Near-Inertial Energy Fluxes

Despite there being comparable energy in the near-inertial and semidiurnal kinetic energy spectra (Figures 4b and 4e), the much smaller density and therefore pressure perturbations in the near-inertial wave band result in energy fluxes being an order of magnitude weaker than those generated by the M_2 internal tide. This order of magnitude difference is consistent with analysis from the New England Shelf by MacKinnon and Gregg [2003b].

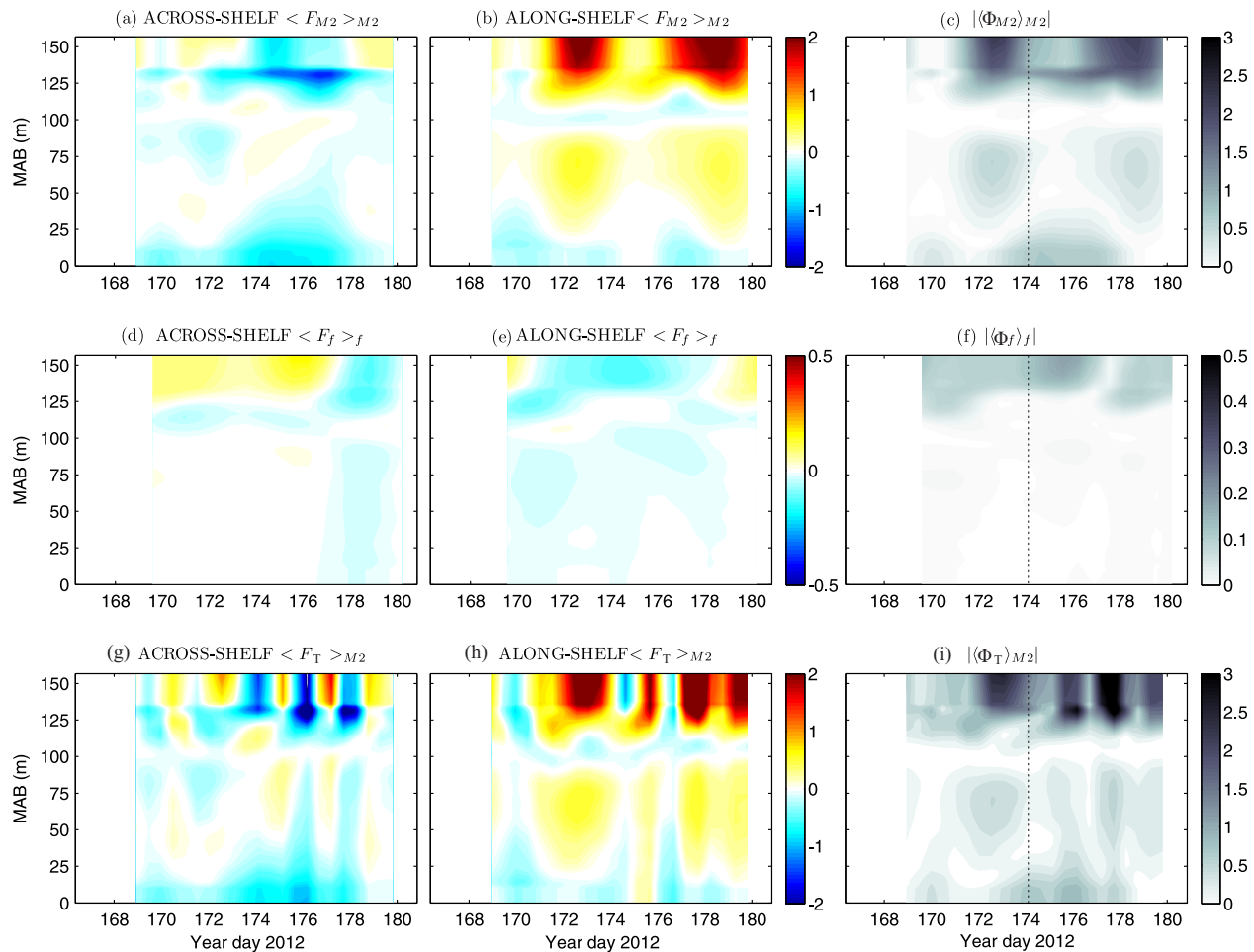


Figure 7. (a, d, and g) Across and (b, e, and h) along-shelf energy fluxes at ST4. (c, f, and i) Magnitude of flux vectors (W m^{-2}). Semidiurnal (Figures 7a–7c), near-inertial (Figures 7d–7f), near-inertial to semidiurnal (Figures 7g–7i). Note changes in the color scales. Vertical lines mark spring tides.

The depth-integrated deployment mean across-shelf fluxes at ST4 and ST5 are 1 and -6 W m^{-1} , respectively (Table 3), and are focused in the surface mixed layer (Figures 7d, 7f, 8d, and 8f). Considering only positive across-shelf fluxes, then shoreward near-inertial energy transport averaged 4 and 9 W m^{-1} at each site. The weaker flux at ST4 tallies with the reduced level of inertial kinetic energy seen in Figure 5c.

5.3. Combined Near-Inertial and Tidal Flux

In order to assess whether or not energy input into the surface by wind events modifies baroclinic internal wave energy transport, fluxes within the combined f -to- M_2 frequency band (Φ_T) were computed. Considering solely the deployment mean depth integrals (Table 3), it would at first appear that the inertial oscillations have a minimal impact. Since the net cross terms in equation (5) are zero with respect to the full depth and time integral, $\int_0^t \int_{-H}^0 \Phi_T dz dt = \int_0^t \int_{-H}^0 \Phi_{M_2} dz dt + \int_0^t \int_{-H}^0 \Phi_f dz dt$, and given the order of amplitude difference between Φ_{M_2} and Φ_f , the strength and direction of $\int_0^t \int_{-H}^0 \Phi_T dz dt$ is dominated by the semidiurnal contribution. However, these net fluxes mask (a) the true temporal variability and (b) an overall increase in energy being moved around the system.

Post day 175, the magnitude of $\int_{-H}^0 \langle \Phi_T \rangle_{M_2} dz$ increases significantly compared to the solely tidally driven flux (Figures 9a and 9b). Toward the end of day 177 at ST4, an extra 80 W m^{-1} is attained over one tidal period, corresponding to a 50% increase in the flux. Similarly at ST5, there is more than a 50% increase in flux on day 176. In contrast, when semidiurnal motions dominate the residual currents between days 171 and 174 (Figures 3a and 3b), there is no increase in flux magnitude. The extra energy within Φ_T is distributed fully around 360° (Figure 6d), visually demonstrating how the depth and time integral of the cross

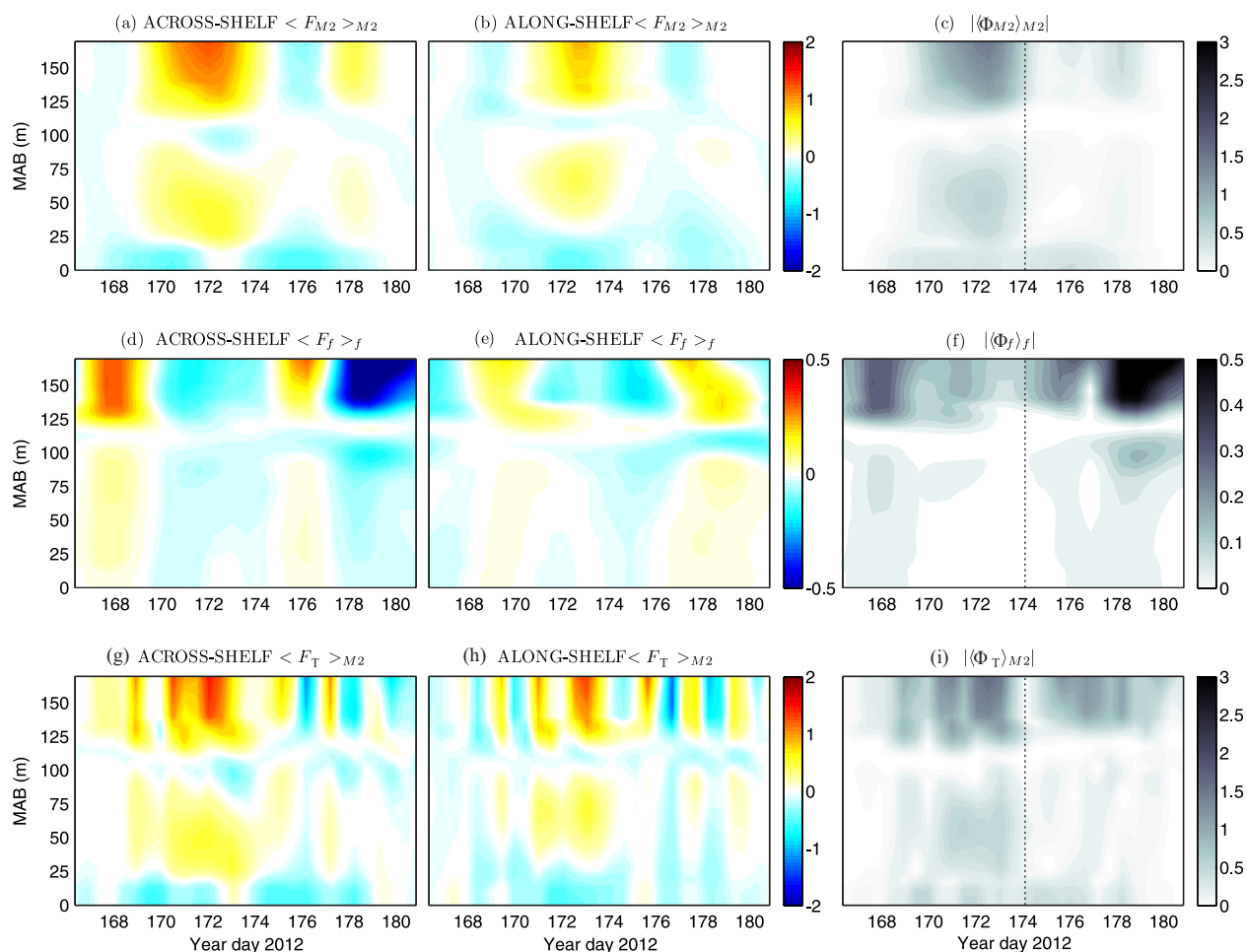


Figure 8. (a, d, and g) Across and (b, e, and h) along-shelf energy fluxes at ST5. (c, f, and i) magnitude of flux vectors (W m^{-2}). Semidiurnal (Figures 8a–8c), near-inertial (Figures 8d–8f), near-inertial to semidiurnal (Figures 8g–8i). Note changes in the color scales. Vertical lines mark spring tides.

terms are zero. There is an approximate 2 day counter-clockwise beating to Φ_T that is felt throughout the entire water column (Figures 9c), although the three-layer vertical structure is maintained (Figures 7i and 8i). Relative to Φ_{M_2} , this beat and increase in flux magnitude explains an additional O(10%) of the variance of the full flux time series (Φ) and is most noticeable post day 174.

Further evidence for extra energy being moved around within the system is found by looking at the spectra of instantaneous fluxes (Figure 10). There is a broad primary peak in clockwise energy between M_4 and the interaction frequency $M_2 + f$. Instantaneous energy flux induced by the semidiurnal tide alone accounts for the peak at M_4 ($2 \times M_2$ periods), since M_2 variability in pressure is 90° out of phase with semidiurnal velocities. The remainder of the peak near $M_2 + f$ is captured by including the near-inertial band of the internal wave spectrum. Note that $\Phi_{M_2} + \Phi_f$ does not replicate this peak since it comes from the cross terms in equation (5). The 2 day counter-clockwise beat is also fully captured by Φ_T and is very close to the inertial-tidal interaction frequency of 2.3 days ($M_2 - f$).

As is often the case in shelf sea environments, we are primarily concerned with the on-shelf supply (and dissipation) of energy. Isolating only positive instances of F_u , inclusion of near-inertial motion increases on-shelf energy fluxes by 43% and 25% at ST4 and ST5 to 40 and 60 W m^{-1} , respectively (Table 3).

6. Discussion

6.1. Generation and Propagation of the M_2 IT

Owing to the highly complex bathymetry, barotropic to baroclinic tidal energy conversion along the Celtic Sea shelf edge is exceptionally variable, both spatially and temporally. Using moorings deployed at

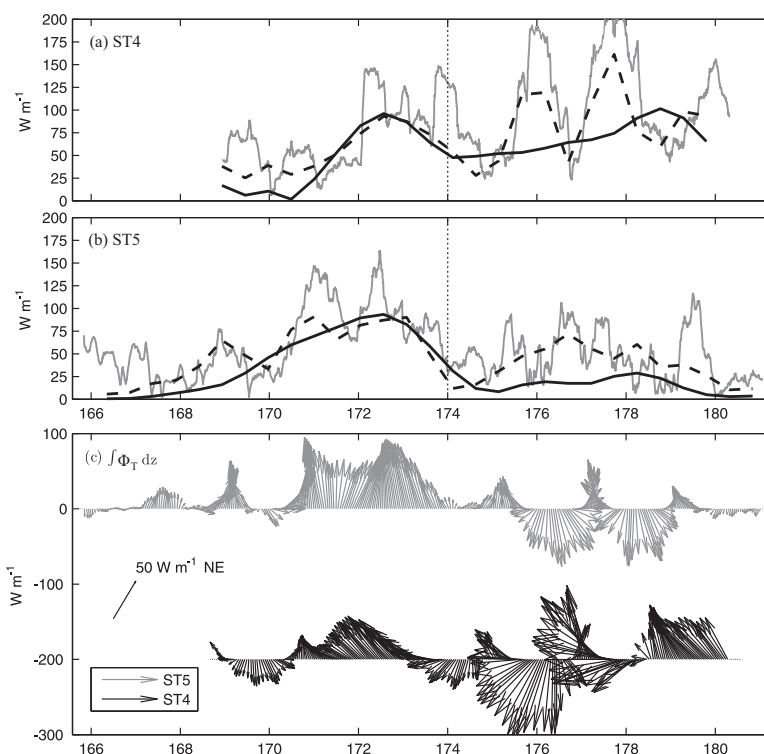


Figure 9. Magnitude of depth-integrated energy flux vectors (W m^{-1}) at (a) ST4 and (b) ST5. $|\int_{-H}^0 \langle \Phi_{M2} \rangle_{M2} dz|$ (thick solid line), $|\int_{-H}^0 \langle \Phi_T \rangle_{M2} dz|$ (dashed line), 12.42 h running average of total instantaneous energy flux magnitude, $|\int_{-H}^0 \Phi dz|$ (thin gray line). Vertical lines mark spring tides. (c) Vectors of instantaneous depth-integrated Φ_T energy smoothed with a running 12.42 h window. Note that ST4 and ST5 are offset by -200 W m^{-1} .

the shelf edge and on the steep slope during this same June 2012 cruise, *Vlasenko et al.* [2014] validate a model that pin-points internal tidal generation hot spots at the end of the headland and within the canyons either side. The wave systems generated propagate in all directions, on, off, and along shelf. In light of this, the 90° difference in M_2 flux direction between ST4 and ST5 (Figure 6c) is not surprising, with both sites likely to receive energy from multiple wave packets generated from different locations.

The mismatch between internal tide activity and the spring-neap cycle has been reported elsewhere. Remotely (as opposed to locally) generated internal waves propagating across the shelf break [*Nash et al.*, 2012], superposition of waves from multiple sources [*Duda et al.*, 2013], and wave-wave interactions are all processes that introduce unpredictability into the direction and timing of the internal tide. Changes in shelf break criticality in response to varying stratification (G. R. Stephenson et al., Storms modify baroclinic energy transport at the Celtic Sea shelf break: changes in stratification, submitted to *Geophysical Research Letters*, 2014), and advection by tide, wind, and mesoscale density-driven currents are also factors that would disrupt any expected spring-neap flux persistence.

Comparison of our flux estimates to previous studies must be done with care. *Green et al.* [2008] use data collected from a mooring located right on the shelf edge (in 200 m of water), in between ST4 and ST5 (marked in Figure 1b). Their estimates are therefore likely to include significant amounts of energy from high-frequency waves that dissipate quickly and fluxes parallel to the shelf related to long-slope jet-like currents interacting with the topography [*Holt and Thorpe*, 1997]. Furthermore, they do not perform any filtering to isolate semidiurnal perturbations. Instead, their flux estimates are derived from a 12.5 h moving average window applied to unfiltered estimates of $u'p'$ (comparable to the running averages plotted in Figures 9a and 9b), and therefore represent the complete linear internal wavefield energy flux. We must therefore compare their results with F , our full baroclinic flux estimates, rather than F_{M2} . They estimate a 73 W m^{-1} on-shelf flux and conclude that this decreases to zero within 20–30 km of the shelf break, a finding that, like *Inall et al.* [2011], we can not support. The comparable positive (shoreward) fluxes at our moorings,

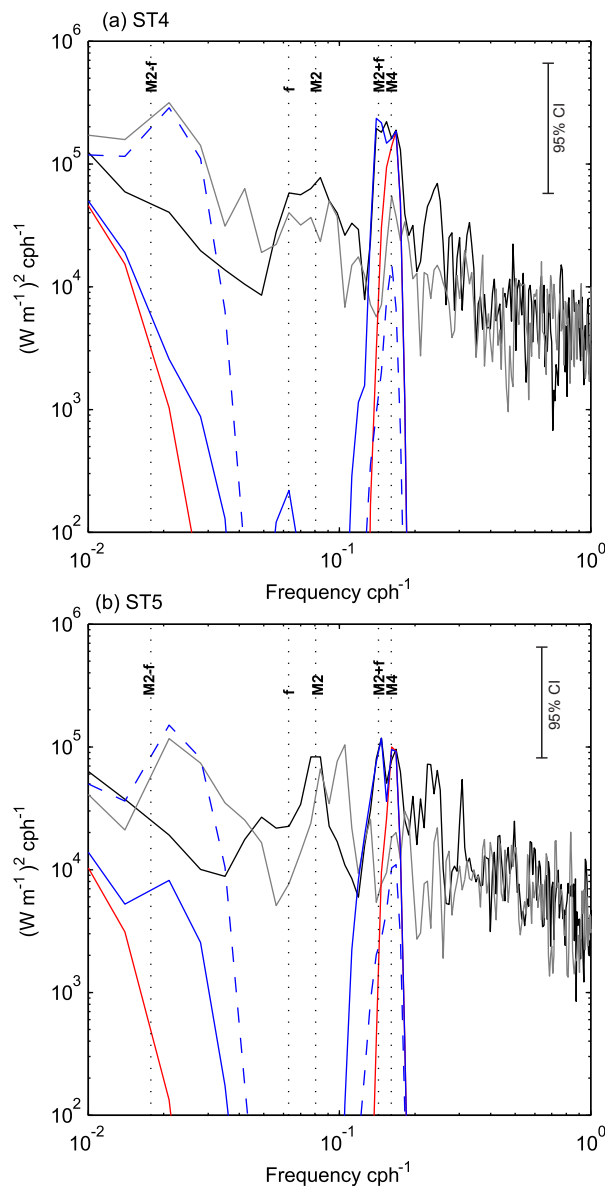


Figure 10. Rotary power spectra of instantaneous depth-integrated vector fluxes at (a) ST4 and (b) ST5. Black (gray) lines are the clockwise (counter-clockwise) components of $\int_{-H}^0 \Phi dz$. Red line is the clockwise component of $\int_{-H}^0 \Phi_{M2} dz$. Solid (dashed) blue lines are the clockwise (counter-clockwise) components of $\int_{-H}^0 \Phi_T dz$. Vertical dotted lines mark the inertial, tidal, and interaction frequencies.

calculated from observations made sufficiently far from the shelf edge, the full internal wavefield drives a $130 W m^{-1}$ flux on-shelf, half of which is from the semidiurnal wave band [Mackinnon and Gregg, 2003b]. In the Southern California Bight, a much weaker $2.3 W m^{-1}$ cross-shelf flux is sustained by the semidiurnal internal tide [Lucas et al., 2011], calculated by band pass filtering the perturbation quantities and therefore comparable to our F_{M2} quantities.

6.2. Energy Dissipation

Since we do not have information on the density structure at ST3, we are unable to calculate energy dissipation (ϵ) from the flux divergence. However, since the total inertial and semidiurnal energies ($E = KE + PE$) at ST4 and ST5 are known, we can estimate the total energy at ST3 by assuming that the same PE:KE ratios are applicable. The potential energy (PE) is calculated within 58 h windows from:

located 30–40 km from the 200 m depth contour and therefore outside of the complex shelf edge generation zone, average 93 and $118 W m^{-1}$ at ST4 and ST5, respectively (Table 3).

Other studies suggest that onshore flux estimates for the Celtic Sea region span an order of magnitude: $73 W m^{-1}$ [Green et al., 2008], $100 W m^{-1}$ [Holt and Thorpe, 1997], $163 W m^{-1}$ [Baines, 1982], and $940 W m^{-1}$ [Inall et al., 2011], a likely consequence of the high variability in the internal tidal generation force, three-dimensional wave propagation, and differing duration and location of observations. Our estimates sit within the lower half of this range, but having been made outside of the internal tidal generation zone, we believe to be one of the best estimates to date of the internal wave energy that finally propagates into the interior of the Celtic Sea shelf once the lower-mode longer wavelength internal tide has been properly established. For comparison, tidally averaged full baroclinic energy fluxes generated in the interior of the Celtic Sea by local topographic rises (as opposed to at the shelf edge some 300 km away) average $14.2 W m^{-1}$ [Palmer et al., 2008].

Looking elsewhere on the Northwest European Shelf, an on-shelf flux of $104 W m^{-1}$ has been observed on the Malin Shelf [Sherwin, 1988], and $140 W m^{-1}$ in the Faroe-Shetland Channel [Hall et al., 2011], although the same caveat of a mooring location near the shelf edge also applies to these studies. Elsewhere in the world, at the New Jersey Shelf, and

$$PE(z) = \frac{1}{4} N(z)^2 \rho(z) \eta_0(z)^2, \quad (6)$$

where $\eta_0(z)$, the vertical elevation amplitude within each window is derived according to $\Delta\rho_0/\frac{\Delta\rho}{\Delta z}$ with $\Delta\rho_0$ the amplitude of M_2 density oscillations at height z and $\frac{\Delta\rho}{\Delta z}$ the local value of the vertical density gradient. Given a distance of 45 km between the mooring sites, a mean water depth of 150 m, a wave propagation speed of 0.5 m s^{-1} , and assuming direct on-shelf propagation, turbulent dissipation during the poststorm period (days 170.5–173.5) averaged $3.6\text{--}4.3 \times 10^{-5} \text{ W m}^{-3}$. After restratification, the average dissipation at both sites was $1.6 \times 10^{-4} \text{ W m}^{-3}$ (days 175–178). These values sit toward the lower end of previously estimated and directly measured dissipation rates [Inall *et al.*, 2011; Sharples *et al.*, 2007]. However, they are approximately double the average pycnocline dissipation rates calculated from microstructure measurements made half way between moorings ST3 and ST4 (M. R. Palmer *et al.*, Turbulence and mixing by internal waves in the Celtic Sea determined from ocean glider microstructure measurements, submitted to *Journal of Marine Systems*, 2014), $1.9 \times 10^{-5} \text{ W m}^{-3}$ (days 170.5–173.5) and $4.9 \times 10^{-5} \text{ W m}^{-3}$ (days 175–178). This suggests that a significant amount of baroclinic energy loss takes place at the seabed and also implies that dissipation rates decrease with distance from the generation site.

Taking the maximum positive on-shelf flux within the f -to- M_2 band (183 W m^{-1} , Table 3), and our lower estimate of dissipation (assuming that it is more representative of energy losses away from the more dynamic shelf edge), without any further input or interactions energy at ST4 and ST5 may travel another 35 km further onto the shelf—a minimum propagation of $O(75) \text{ km}$ from the generation site. These calculations have been done on the basis of energy and dissipation within the linear f -to- M_2 internal wave band alone and have necessitated some knowingly flawed assumptions. Nevertheless, our energy decay length scale sits in between the extremes previously reported by Green *et al.* [2008] and Inall *et al.* [2011]. Given the highly complex wavefield in this area however, and having not captured contributions from the nonhydrostatic waves, confident closure of an energy-dissipation budget would be unrealistic. Although a useful guide, these bulk estimates, that are so often made, mask the true episodic nature of dissipation and mixing in shelf seas.

6.3. Near-Inertial and Tidal Interaction

Explicit consideration of the cross terms in equation (5) facilitates an understanding of the physical mechanism increasing horizontal fluxes of energy following the development of wind-driven inertial oscillations. Taking the across-shelf component at ST5 as an example (Figure 11), the term $u'_f p'_{M_2}$, formed from correlations between the near-inertial velocity and semidiurnal pressure perturbations, is equivalent in magnitude to $u'_{M_2} p'_{M_2}$. It has the periodicity of the $M_2 + f$ interaction frequency ($\approx 6.98 \text{ h}$). We propose that the dominant physical mechanism behind the importance of this term is a coupling between vertical shear from wind-induced oscillations and vertical velocities associated with the M_2 internal tide. The coupling is represented by the vertical nonlinear momentum terms in the equations of motion. The horizontal components of particle acceleration, $\frac{du}{dt}$ and $\frac{dv}{dt}$ in full are:

$$\frac{du}{dt} = \frac{\partial u}{\partial t} + u \frac{\partial u}{\partial x} + v \frac{\partial u}{\partial y} + w \frac{\partial u}{\partial z}, \quad (7)$$

$$\frac{dv}{dt} = \frac{\partial v}{\partial t} + u \frac{\partial v}{\partial x} + v \frac{\partial v}{\partial y} + w \frac{\partial v}{\partial z}, \quad (8)$$

where the last terms on the RHS account for accelerations resulting from interaction between a vertical velocity and a vertical current shear. Attributing specific processes to these motions, namely vertical velocities associated with the M_2 internal tide (w_{M_2}) and inertial current shear ($\frac{du}{dz}$), their product $w_{M_2} \frac{du}{dz}$ is logarithmically proportional to $u'_f p'_{M_2}$. Internal tidal pressure variability, p'_{M_2} , and vertical velocities, w_{M_2} , are both derived from semidiurnal density perturbations, ρ'_{M_2} . The former from equation (2), and the latter via $w_{M_2} = \frac{d\zeta}{dt}$ where ζ , the vertical isopycnal displacement of the semidiurnal tide is derived from $\zeta = -\rho'_{M_2} \left(\frac{\partial \rho}{\partial z}\right)^{-1}$. As the pressure (p'_{M_2}) and density (ρ'_{M_2}) perturbations increase, so do the isopycnal excursions and therefore also the associated vertical velocities. Similarly, as horizontal inertial current perturbations (u'_f) increase so does the vertical shear of those oscillations, $\frac{du}{dz}$. Post day 174, where strong internal tidal vertical velocities coincide with high inertial vertical shear around 120 mab (Figure 12), this nonlinear coupling produces energy at the $M_2 + f$ frequency (Figure 10) that is captured in the cross term $u'_f p'_{M_2}$. Using a numerical model, the generation of $M_2 + f$ currents on the Hebrides shelf was attributed to this interaction

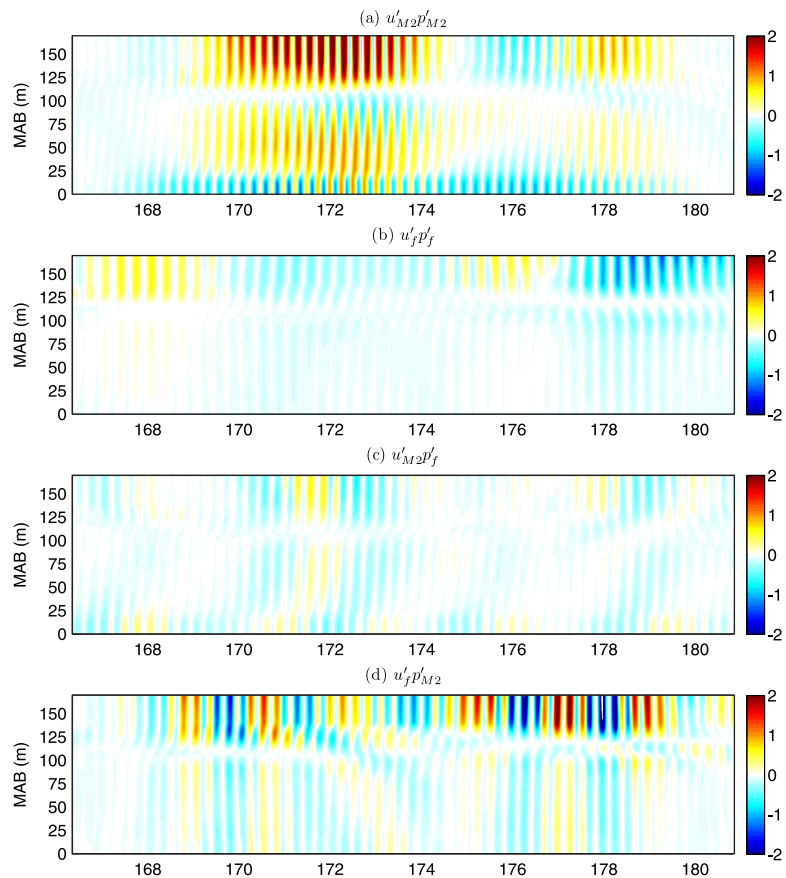


Figure 11. Contributing terms to ST5 cross-shelf F_T energy flux ($W m^{-2}$). (a) $u'_{M2}p'_{M2}$, (b) $u'_f p'_f$, (c) $u'_{M2}p'_f$, and (d) $u'_f p'_{M2}$.

[Xing and Davies, 2002; Davies and Xing, 2003]. Additionally, following a typhoon, Guan et al. [2014] credit the occurrence of energy at the sum of the inertial and diurnal frequencies to the nonlinear vertical momentum term.

Calculation of the bulk shear between the upper and lower boundary layers further highlights the role of vertical inertial current shear in the coupling. Taking the $1027 kg m^{-3}$ isopycnal as the center of the pycnocline, the upper and lower-layer depth mean velocity components, (u_s, v_s) and (u_b, v_b) , respectively, are calculated. The bulk shear vector components are then

$$S_u = \frac{u_s - u_b}{0.5h}, S_v = \frac{v_s - v_b}{0.5h}, \tag{9}$$

where h is the total water depth (following Burchard and Rippeth [2009]). The bulk shear vector $\mathbf{S} = S_u + iS_v$, and the bulk shear squared $S^2 = S_u^2 + S_v^2$. From day 175 onward at ST4, maxima in energy flux are perfectly timed with pulses in S^2 on days 176, 177.5, and 179.5 (marked by stars in Figure 13a). At ST5, although not as clear, pulses in energy also coincide with increases and decreases in bulk shear (Figure 13b). Inertial bulk shear is strong, if not dominant, during this latter deployment period (Figure 14). During the first half of the time series (days 171 and 174), when there is little difference between Φ_{M2} and Φ_T (Figure 9), semidiurnal shear, driven by the internal tide dominates. The coincidence of strong inertial shear and an increase in energy fluxes post day 174, following a period of semidiurnal shear prevalence and no corresponding increase in flux, is further supporting evidence for the role of $\frac{du_r}{dz}$ as the physical coupling mechanism between inertial and tidal energy. Without strong vertical inertial shear, energy from the wind can not be transferred into the internal wavefield.

The approximate 2 day beating, very close to the $M_2 - f$ frequency, is not due to nonlinear interaction, and no energy is carried at this frequency. It is simply the result of the two frequencies, f and M_2 , moving in and out of phase with each other. On its own this does not generate the additional energy at $M_2 + f$, but can be

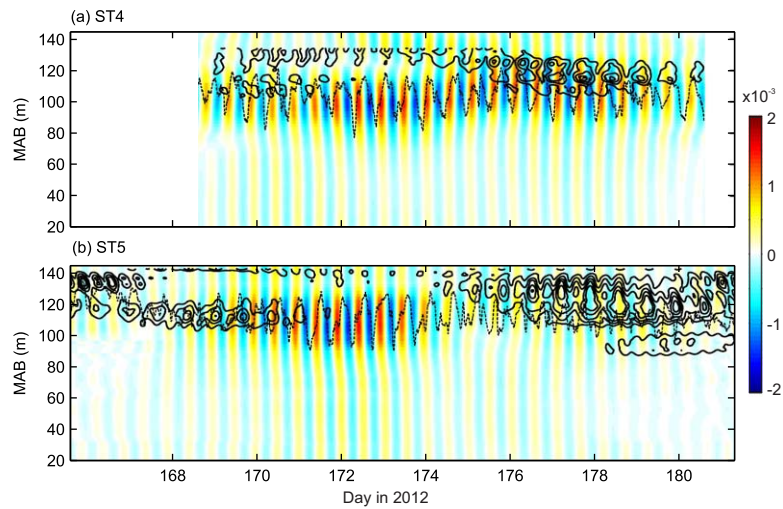


Figure 12. (a) Semidiurnal internal tide vertical velocities w_{M2} in $m\ s^{-1}$ (shading) calculated from vertical isopycnal displacements plotted against vertical inertial current shear $(\frac{du}{dz})^2 + (\frac{dv}{dz})^2$ in s^{-2} (black contours of 2, 4, 6, 8, and 10×10^{-5}) at ST4. Dashed contour is the $1027\ kg\ m^{-3}$ isopycnal. (b) As above for ST5.

thought of as phasing that determines whether the nonlinearly generated flux captured by the cross terms makes a constructive or destructive contribution with respect to the semidiurnal tide. At times marked by the stars in Figure 13a, f and M_2 current oscillations are aligned such that maxima in vertical inertial shear and IT vertical velocities coincide. The magnitude and direction of energy contributed from the subsequent interaction works to positively increase that already being transported by the internal tide. This could be thought of as the internal tide “carrying” the inertial energy (constructive interference). Conversely, it is also possible for internal tidal energy fluxes to be “dampened,” as suggested on day 177 at ST4 (Figure 9a), if the contribution from the nonlinear coupling works against the linear internal tidal component (destructive interference).

6.4. Regime Shifts

The energy fluxes and bulk shear vectors presented here provide some of the first clear evidence of two distinct regimes: tidal and inertial. On day 174, there is a switch from a tidally dominated shear and energy regime to an inertially dominated system. The timing and balance between these two regimes is likely controlled by a variety of interconnected variables: the strength, development and persistence of wind events, the magnitude of the background internal tide, the timing of the spring-neap cycle, and the strength and structure of stratification, both across the shelf and over the shelf break.

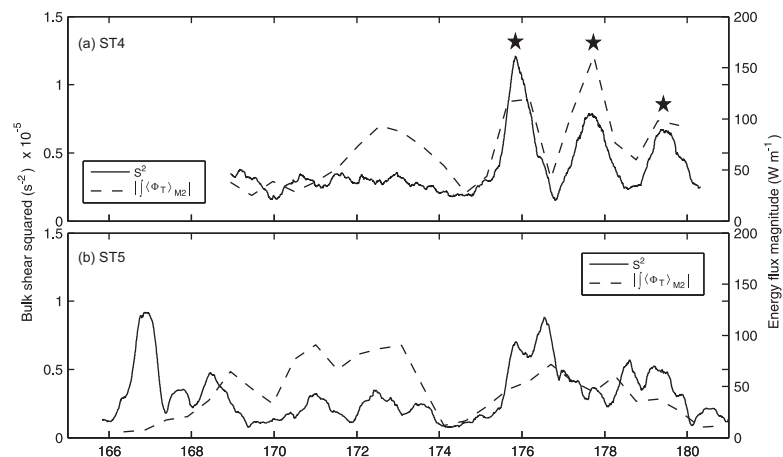


Figure 13. A 12.42 h running mean of the bulk shear squared (S^2) and the magnitude of the depth-integrated energy flux $\langle \Phi_T \rangle_{M2}$ at (a) ST4 and (b) ST5. Stars in Figure 13a highlight clear coincidence of peaks in bulk shear and energy flux.

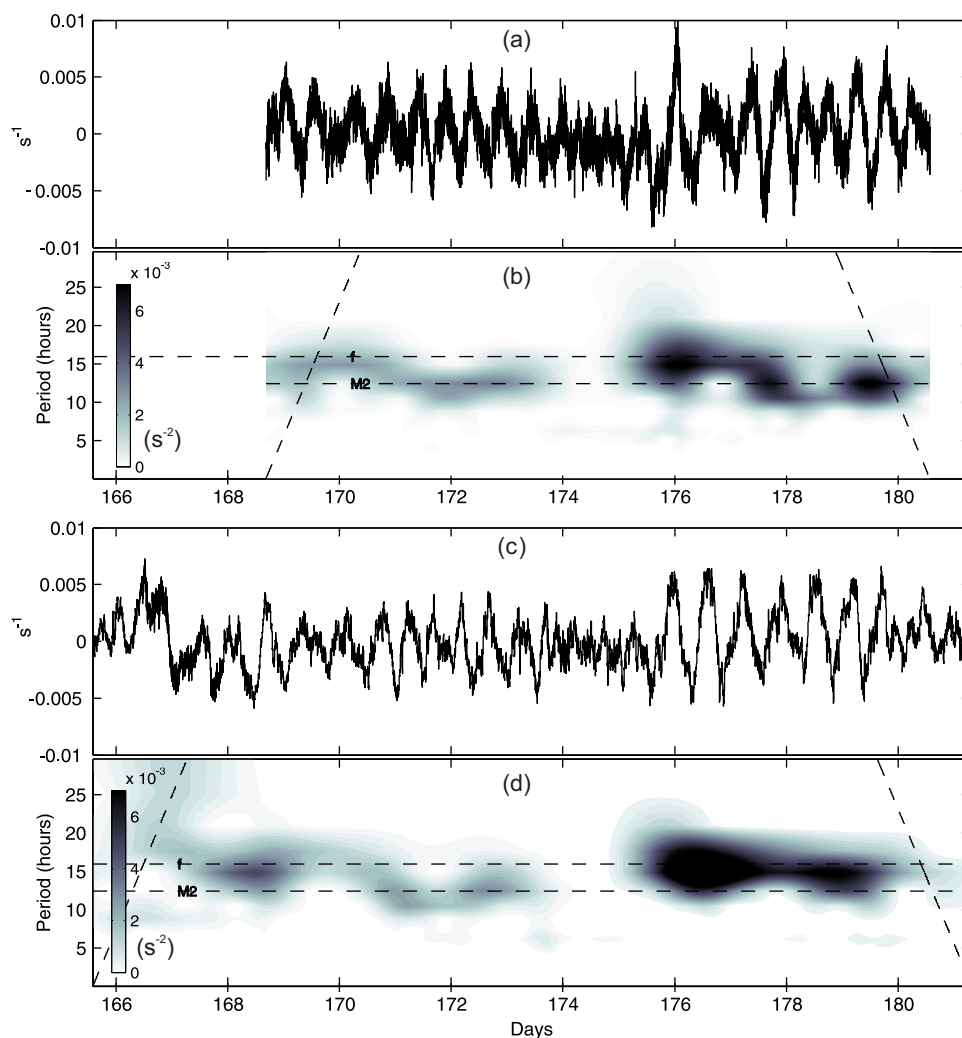


Figure 14. (a) Clockwise bulk shear (s^{-1}) at ST4. (b) Wavelet power spectrum of clockwise bulk shear at ST4 (s^{-2}). The near vertical dashed lines mark the Cone of Influence, outside of which calculation of the power becomes uncertain. (c and d) For ST5.

The tidal regime between days 170 and 174 follows a prolonged and intense storm that failed to excite especially strong or long-lasting inertial oscillations. Instead, elevated wind stress acts to significantly deepen the surface mixed layer and tighten the pycnocline. In contrast, the inertial regime from day 174 onward is triggered by a sudden and short-lived storm (comparable to the local inertial period) that initiated strong inertial oscillations and increased inertial kinetic energy throughout the water column. During this time, nonlinear inertial-tidal interaction increases the magnitude of energy fluxes and introduces a 2–2.3 day counter-clockwise beating that distributes this energy in all directions, both off, on, and along the shelf.

7. Summary

We demonstrate how wind-generated near-inertial oscillations can modify baroclinic internal wave energy fluxes in a stratified shelf sea environment. Linear fluxes of baroclinic energy in the Celtic Sea are dominated by the semidiurnal tide, that outside of the complex generation zone drives $28\text{--}48\text{ W m}^{-1}$ directly onto the shelf. Given the complex three-dimensional nature of the generation and propagation, however, spatial variability is high and net flux vectors may differ by 90° or more within an IT wavelength. Horizontal energy fluxes driven independently by near-inertial motions are an order of magnitude weaker, but nonlinear interaction between the vertical shear of inertial-oscillations and the vertical velocity associated with the M_2 internal tide is a significant source of energy at the sum of their frequencies ($M_2 + f$). The phase relationship between M_2 and f determines whether this nonlinear interaction constructively enhances or destructively dampens the linear tidal component of the flux, a phasing that introduces a 2–2.3 day counter-clockwise

beating to the energy transport. Relative to the M_2 contribution, this beating and increase in flux magnitude explains an additional 10% of the variability of the full flux time series (not accounting for the high-frequency, nonhydrostatic component). Over individual tidal periods, inertial-tidal interaction resulted in a 50% increase in flux magnitude. Over the whole deployment, a 25–43% increase in positive on-shelf energy flux was observed. Our data set clearly identifies a switch between tidal and inertially dominated shear and energy flux regimes. These findings are highly relevant in the much needed development of mixing parameterizations for shelf sea models where nonlinear interactions and the processes driving temporal and spatial variability of shear, instability and consequently turbulence are of importance. Failure to represent the inertial-tidal interactions described here will lead to underestimation of the magnitude and episodic nature of turbulent dissipation and thermocline mixing.

Acknowledgments

This was funded by NERC grant NE/I030224/1 (FASTNET project). M. Green was supported by a NERC Advanced Fellowship (NE/F014821/1). The authors wish to thank the crew of the RV Discovery, Colin Griffiths, Estelle Dumont, Terry Doyle, and the NMF-SS staff for their assistance in collecting these data sets. Thanks also to Tom Rippeth for useful discussions and to the anonymous reviewers whose feedback helped improved this work. Data used in this study are available through the British Oceanographic Data Centre (<http://www.bodc.ac.uk/>).

References

- Alford, M. H. (2001), Fine-structure contamination: Observations and a model of a simple two-wave case, *J. Phys. Oceanogr.*, *31*(9), 2645–2649.
- Alford, M. H. (2003), Redistribution of energy available for ocean mixing by long-range propagation of internal waves, *Nature*, *423*(6936), 159–162.
- Alford, M. H., M. F. Cronin, and J. M. Klymak (2012), Annual cycle and depth penetration of wind-generated near-inertial internal waves at Ocean Station Papa in the Northeast Pacific, *J. Phys. Oceanogr.*, *42*(6), 889–909.
- Baines, P. G. (1982), On internal tide generation models, *Deep Sea Res., Part A*, *29*(3), 307–338.
- Borges, A. V., B. Delille, and M. Frankignoulle (2005), Budgeting sinks and sources of CO_2 in the coastal ocean: Diversity of ecosystems counts, *Geophys. Res. Lett.*, *32*, L14601, doi:10.1029/2005GL023053.
- Burchard, H., and T. P. Rippeth (2009), Generation of bulk shear spikes in shallow stratified tidal seas, *J. Phys. Oceanogr.*, *39*(4), 969–985, doi:10.1175/2008jpo4074.1.
- Carter, G. S., M. A. Merrifield, J. M. Becker, K. Katsumata, M. C. Gregg, D. S. Luther, M. D. Levine, T. J. Boyd, and Y. L. Firing (2008), Energetics of M_2 barotropic-to-baroclinic tidal conversion at the Hawaiian Islands, *J. Phys. Oceanogr.*, *38*(10), 2205–2223, doi:10.1175/2008jpo3860.1.
- Davies, A. M., and J. X. Xing (2003), On the interaction between internal tides and wind-induced near-inertial currents at the shelf edge, *J. Geophys. Res.*, *108*(C3), 3099, doi:10.1029/2002JC001375.
- Duda, T. F., A. E. Newhall, G. Gawarkiewicz, M. J. Caruso, H. C. Graber, Y. J. Yang, and S. Jan (2013), Significant internal waves and internal tides measured northeast of Taiwan, *J. Mar. Res.*, *71*, 47–82.
- Egbert, G. D., and R. D. Ray (2001), Estimates of M_2 tidal energy dissipation from Topex/Poseidon altimeter data, *J. Geophys. Res.*, *106*, 22,475–22,502.
- Garrett, C. (2001), What is the near-inertial band and why is it different from the rest of the internal wave spectrum?, *J. Phys. Oceanogr.*, *31*(4), 962–971.
- Garrett, C. (2003), Internal tides and ocean mixing, *Science*, *301*, 1858–1859.
- Green, J. A. M., J. H. Simpson, S. Legg, and M. R. Palmer (2008), Internal waves, baroclinic energy fluxes and mixing at the European shelf edge, *Cont. Shelf Res.*, *28*(7), 937–950, doi:10.1016/j.csr.2008.01.014.
- Gregg, M. C. (1989), Scaling turbulent dissipation in the thermocline, *J. Geophys. Res.*, *94*, 9686–9698, doi:10.1029/JC094iC07p09686.
- Guan, S., W. Zhao, J. Huthnance, J. Tian, and J. Wang (2014), Observed upper ocean response to typhoon Megi (2010) in the Northern South China Sea, *J. Geophys. Res. Oceans*, *119*, 3134–3157, doi:10.1002/2013JC009661.
- Hall, R. A., J. M. Huthnance, and R. G. Williams (2011), Internal tides, nonlinear internal wave trains, and mixing in the Faroe-Shetland Channel, *J. Geophys. Res.*, *116*, C03008, doi:10.1029/2010JC006213.
- Holloway, P. E. (2001), A regional model of the semidiurnal internal tide on the Australian North West Shelf, *J. Geophys. Res.*, *106*, 19,625–19,638, doi:10.1029/2000JC000675.
- Holt, J. T., and S. A. Thorpe (1997), The propagation of high frequency internal waves in the Celtic Sea, *Deep Sea Res., Part I*, *44*(12), 2087–2116.
- Holtermann, P. L., and L. Umlauf (2012), The Baltic Sea tracer release experiment: 2. Mixing processes, *J. Geophys. Res.*, *117*, C01022, doi:10.1029/2011JC007445.
- Inall, M., D. Aleynik, T. Boyd, M. Palmer, and J. Sharples (2011), Internal tide coherence and decay over a wide shelf sea, *Geophys. Res. Lett.*, *38*, L23607, doi:10.1029/2011GL049943.
- Kang, D., and O. Fringer (2012), Energetics of barotropic and baroclinic tides in the Monterey Bay Area, *J. Phys. Oceanogr.*, *42*(2), 272–290, doi:10.1175/jpo-d-11-039.1.
- Lee, C. M., E. Kunze, T. B. Sanford, J. D. Nash, M. A. Merrifield, and P. E. Holloway (2006), Internal tides and turbulence along the 3000-m isobath of the Hawaiian Ridge, *J. Phys. Oceanogr.*, *36*(6), 1165–1183.
- Lien, R. C., T. Y. Tang, M. H. Chang, and E. A. D'Asaro (2005), Energy of nonlinear internal waves in the South China Sea, *Geophys. Res. Lett.*, *32*, L05615, doi:10.1029/2004GL022012.
- Lucas, A. J., P. J. S. Franks, and C. L. Dupont (2011), Horizontal internal-tide fluxes support elevated phytoplankton productivity over the inner continental shelf, *Limnol. Oceanogr. Methods*, *1*, 56–74.
- MacKinnon, J. A., and M. C. Gregg (2003a), Mixing on the late-summer New England shelf—Solibores, shear, and stratification, *J. Phys. Oceanogr.*, *33*(7), 1476–1492.
- MacKinnon, J. A., and M. C. Gregg (2003b), Shear and baroclinic energy flux on the summer New England shelf, *J. Phys. Oceanogr.*, *33*(7), 1462–1475.
- Mihaly, S. F., R. E. Thomson, and A. B. Rabinovich (1998), Evidence for nonlinear interaction between internal waves of inertial and semidiurnal frequency, *Geophys. Res. Lett.*, *25*, 1205–1208, doi:10.1029/98GL007722.
- Muller, P., G. Holloway, F. Henyey, and N. Pomphrey (1986), Nonlinear interactions among internal gravity waves, *Rev. Geophys.*, *24*, 493–536, doi:10.1029/RG024i003p00493.
- Muller-Karger, F. E., R. Varela, R. Thunell, R. Luerssen, C. M. Hu, and J. J. Walsh (2005), The importance of continental margins in the global carbon cycle, *Geophys. Res. Lett.*, *32*, L01602, doi:10.1029/2004GL021346.

- Munk, W., and C. Wunsch (1998), Abyssal recipes II: Energetics of tidal and wind mixing, *Deep Sea Res., Part I*, 45(12), 1977–2010.
- Nash, J. D., M. H. Alford, and E. Kunze (2005), Estimating internal wave energy fluxes in the ocean, *J. Atmos. Oceanic Technol.*, 22(10), 1551–1570, doi:10.1175/jtech1784.1.
- Nash, J. D., S. M. Kelly, E. L. Shroyer, J. N. Moum, and T. F. Duda (2012), The unpredictable nature of internal tides on continental shelves, *J. Phys. Oceanogr.*, 42(11), 1981–2000, doi:10.1175/jpo-d-12-028.1.
- Palmer, M. R., T. P. Rippeth, and J. H. Simpson (2008), An investigation of internal mixing in a seasonally stratified shelf sea, *J. Geophys. Res.*, 113, C12005, doi:10.1029/2007JC004531.
- Pingree, R. D., and G. T. Mardell (1981), Slope turbulence, internal waves and phytoplankton growth at the Celtic Sea shelf-break, *Philos. Trans. R. Soc. London A*, 302(1472), 663–682, doi:10.1098/rsta.1981.0191.
- Polzin, K. L., J. M. Toole, and R. W. Schmitt (1995), Finescale parameterizations of turbulent dissipation, *J. Phys. Oceanogr.*, 25(3), 306–328, doi:10.1175/1520-0485(1995)025<0306:FPOTD>2.0.CO;2.
- Ramp, S. R., Y. J. Yang, and F. L. Bahr (2010), Characterizing the nonlinear internal wave climate in the northeastern South China Sea, *Nonlinear Processes Geophys.*, 17(5), 481–498, doi:10.5194/npg-17-481-2010.
- Rippeth, T. P., and M. E. Inall (2002), Observations of the internal tide and associated mixing across the Malin Shelf, *J. Geophys. Res.*, 107(C4), doi:10.1029/2000JC000761.
- Rippeth, T. P., J. H. Simpson, R. J. Player, and M. Garcia (2002), Current oscillations in the diurnal-inertial band on the Catalanian shelf in spring, *Cont. Shelf Res.*, 22(2), 247–265.
- Rippeth, T. P., P. Wiles, M. R. Palmer, J. Sharples, and J. Tweddle (2009), The diapycnal nutrient flux and shear-induced diapycnal mixing in the seasonally stratified western Irish Sea, *Cont. Shelf Res.*, 29(13), 1580–1587, doi:10.1016/j.csr.2009.04.009.
- Sharples, J., C. M. Moore, and E. R. Abraham (2001), Internal tide dissipation, mixing, and vertical nitrate flux at the shelf edge of NE New Zealand, *J. Geophys. Res.*, 106, 14,069–14,081, doi:10.1029/2000JC000604.
- Sharples, J., et al. (2007), Spring-neap modulation of internal tide mixing and vertical nitrate fluxes at a shelf edge in summer, *Limnol. Oceanogr. Methods*, 52(5), 1735–1747, doi:10.4319/lo.2007.52.5.1735.
- Sherwin, T. J. (1988), Analysis of an internal tide observed on the Malin Shelf, north of Ireland, *J. Phys. Oceanogr.*, 18(7), 1035–1050.
- Shroyer, E. L., J. N. Moum, and J. D. Nash (2010), Energy transformations and dissipation of nonlinear internal waves over New Jersey's continental shelf, *Nonlinear Processes Geophys.*, 17(4), 345–360.
- Shroyer, E. L., J. N. Moum, and J. D. Nash (2011), Nonlinear internal waves over New Jersey's continental shelf, *J. Geophys. Res.*, 116, C03022, doi:10.1029/2010JC006332.
- Thomas, H., Y. Bozec, K. Elkalay, and H. J. W. de Baar (2004), Enhanced open ocean storage of CO₂ from shelf sea pumping, *Science*, 304(5673), 1005–1008, doi:10.1126/science.1095491.
- Tintore, J., D. P. Wang, E. Garcia, and A. Viudez (1995), Near-inertial motions in the coastal ocean, *J. Mar. Syst.*, 6(4), 301–312.
- van der Lee, E. M., and L. Umlauf (2011), Internal wave mixing in the Baltic Sea: Near-inertial waves in the absence of tides, *J. Geophys. Res.*, 116, C10016, doi:10.1029/2011JC007072.
- van Haren, H. (2004), Bandwidth similarity at inertial and tidal frequencies in kinetic energy spectra from the Bay of Biscay, *Deep Sea Res., Part I*, 51(5), 637–652, doi:10.1016/j.dsr.2004.01.006.
- van Haren, H., L. Maas, J. T. F. Zimmerman, H. Ridderinkhof, and H. Malschaert (1999), Strong inertial currents and marginal internal wave stability in the central North Sea, *Geophys. Res. Lett.*, 26, 2993–2996, doi:10.1029/1999GL002352.
- Vlasenko, V., N. Stashchuk, M. E. Inall, and J. E. Hopkins (2014), Tidal energy conversion in a global hotspot: On the 3-D dynamics of baroclinic tides at the Celtic Sea shelf break, *J. Geophys. Res. Oceans*, 119, 3249–3265, doi:10.1002/2013JC009708.
- Williams, C., J. Sharples, C. Mahaffey, and T. Rippeth (2013), Wind-driven nutrient pulses to the subsurface chlorophyll maximum in seasonally stratified shelf seas, *Geophys. Res. Lett.*, 40, 5467–5472, doi:10.1002/2013GL058171.
- Wollast, R. (1998), *Evaluation and Comparison of the Global Carbon Cycle in the Coastal Zone and in the Open Ocean*, vol. 10, pp. 213–252, John Wiley, N. Y.
- Wunsch, C., and R. Ferrari (2004), Vertical mixing, energy and the general circulation of the oceans, *Annu. Rev. Fluid Mech.*, 36, 281–314, doi:10.1146/annurev.fluid.36.050802.122121.
- Xing, J. X., and A. M. Davies (2002), Processes influencing the non-linear interaction between inertial oscillations, near inertial internal waves and internal tides, *Geophys. Res. Lett.*, 29(5), doi:10.1029/2001GL014199.
- Zaragosi, S., J.-F. Bourillet, F. Eynaud, S. Toucanne, B. Denhard, A. Van Toer, and V. Lanfumej (2006), The impact of the last European deglaciation on the deep-sea turbidite systems of the Celtic-Armorican margin (Bay of Biscay), *Geo Mar. Lett.*, 26(6), 317–329.